

Predictions for the clustering properties of the Lyman-alpha Forest - I. One-point statistics

Enrique Gaztañaga¹ and Rupert A. C. Croft²

¹ *Consejo Superior de Investigaciones Científicas (CSIC), Institut d'Estudis Espacials de Catalunya (IEEC), Edf. Nexus-201 - c/ Gran Capitan 2-4, 08034 Barcelona, SPAIN*

² *Astronomy Department, Harvard University, 60 Garden St, Cambridge, MA 01238, USA*

17 August 2021

ABSTRACT

We present predictions for the one-point probability distribution and cumulants of the transmitted QSO flux in the high redshift Lyman- α Forest. We make use of the correlation between the Lyman- α optical depth and the underlying matter density predicted by gravitational instability theory and seen in numerical hydrodynamic simulations. We have modelled the growth of matter fluctuations using the non-linear shear-free dynamics, an approximation which reproduces well the results of perturbation theory for the cumulants in the linear and weakly non-linear clustering regime. As high matter overdensities tend to saturate in spectra, the statistics of the flux distribution are dominated by weakly non-linear overdensities. As a result, our analytic approach can produce accurate predictions, when tested against N-body simulation results, even when the underlying matter field has rms fluctuations larger than unity. Our treatment can be applied to either Gaussian or non-Gaussian initial conditions. Here we concentrate on the former case, but also include a study of a specific non-Gaussian model. We discuss how the methods and predictions we present can be used as a tool to study the generic clustering properties of the Ly α forest at high-redshift. With such an approach, rather than concentrating on simulating specific cosmological models, we may be in the position to directly test our assumptions for the Gaussian nature of the initial conditions, and the gravitational instability origin of structure itself. In a separate paper we present results for two-point statistics.

1 INTRODUCTION

The Ly α forest (Lynds 1971, Sargent et al. 1980, see Rauch 1998 for a review) arises naturally in cosmological structure formation scenarios where gravitational instability acts on small initial density perturbations. In hydrodynamic simulations of such models (Cen et al. 1994, Zhang et al. 1995, Hernquist et al. 1996, Wadsley & Bond 1996, Theuns et al. 1998, see also the analytical modelling of e.g., Bi 1993, Reisenegger and Miralda-Escudé 1995), most of the absorption seen in high redshift QSO spectra is generated by residual neutral hydrogen in a continuous fluctuating photoionized intergalactic medium. In such a picture, absorbing structures have a large physical extent. Observational support for this has come from comparison of the Ly α forest in adjacent QSO lines of sight (Bechtold et al. 1994, Dinshaw et al. 1994, 1995, Crofts & Fang 1998). For matter in this phase, it is predicted and found in simulations that the underlying mass density field at a particular point can be related to the optical depth for Ly α absorption (see e.g., Croft et al. 1997) and hence a directly observable quantity, the transmitted flux in the QSO spectrum.

Much work has been devoted to studying the statistical

properties of the mass density field and the generic predictions of the gravitational instability picture. With the Ly α forest as a probe of the density, we avoid many of the uncertainties associated with the use of the galaxy distribution to test theories. In principle, it should be possible, by combining our theoretical knowledge of gravitational clustering with observations of Ly α absorption, to test the Gaussianity of the initial density field, the picture of Ly α formation, and the gravitational instability scenario itself. In this paper, we will concentrate on one-point statistics, namely the one point probability distribution function (PDF) of the transmitted flux, and its moments. We will use as a tool the spherical collapse or shear-free model for the evolution of density perturbations which Fosalba & Gaztañaga (1998a hereafter FG98, 1998b) have shown to be a good approximation to the growth of clustering in the weakly non-linear regime and which we find works well in the density regime appropriate to the study of the Ly α forest. Two point statistics, which probe the scale dependence of clustering will be examined in an accompanying paper (Gaztañaga & Croft 1999, Paper II).

From observations of the Ly α forest, we can measure the PDF of the flux and its moments. The high resolution

arXiv:astro-ph/9811480v2 23 Sep 1999

spectra of the forest taken by the Keck telescope (Hu et al. 1995, Lu et al. 1996, Rauch et al. 1997, Kirkman & Tytler 1997, Kim et al. 1997) allow us to resolve structure in the flux distribution, and make high precision, shot noise-free measurements of these flux statistics. Here we will use the statistical properties of the matter distribution, $\rho(x)$, to predict these observable quantities.

There are a number of studies which predict the evolution of the clustering of density fluctuations, and in particular of the PDF. The Zel'dovich Approximation (ZA) was used by Kofman et al. (1994). Although the ZA reproduces important aspects of non-linear dynamics, it only results in a poor approximation to the PDF and its moments. This can be quantified by noticing, for example, that the hierarchical skewness $S_3 = \bar{\xi}_3/\bar{\xi}_2^2$ in the ZA is $S_3 = 4$ (at leading order in $\bar{\xi}$) instead of the Perturbation Theory (PT) result $S_3 = 34/7$ (see e.g., Peebles 1980). One way to improve on this is to use the PT cumulants to derive the PDF from the Edgeworth expansion (Juszkiewicz et al. 1995, Bernardeau & Kofman 1995). In this case the PDF is predicted to an accuracy given by order of the cumulants involved. Protogeros & Scherrer (1997) introduced the use of a local Lagrangian mapping (that relates the initial and evolved fluctuation) as a generic way to predict the PDF. In this case, the PDF is obtained simply by applying a change of variables (the mapping) to the PDF of the initial conditions. The best of these two approaches is obtained when the Lagrangian mapping is taken to be that of spherical collapse (FG98), which recovers the PT cumulants to arbitrary order in the weakly non-linear regime. There is yet another possibility, which involves performing a perturbative expansion and directly relating the moments of the flux to the moments of the mass (along the lines proposed in a different context by Fry & Gaztanaga 1993). This approach does not use the density PDF, and could incorporate more exact calculations for the (non-linear) density moments.

Our plan for this paper is as follows. In Section 2 we outline the physical basis for the relation we adopt between Ly α optical depth and the mass distribution. In Section 3 we describe our model for following the evolution of the PDF of the density and flux, using non-linear mapping relations presented in appendix A1. The cumulants of the flux distribution predicted by fully non-linear dynamics are described in Section 4, together with the predictions of perturbation theory. The modelling of the effects of redshift distortions and thermal broadening is also described. In Section 5, we compare our analytical results to those measured from simulated spectra, generated using N-body simulations. In Section 6, we discuss the effects of non-Gaussian initial conditions, the redshift evolution of the one-point flux statistics, and the bias between flux and mass fluctuations. We also compare to other work on the statistics of the Ly α forest flux. Our summary and conclusions form Section 7.

2 LYMAN-ALPHA ABSORPTION AND ITS RELATION TO THE MASS DISTRIBUTION

As mentioned in Section 1, the model we use to relate Ly α absorption to the distribution of mass is motivated by the results of numerical simulations which solve the full equations of hydrodynamics and gravity, some including star forma-

tion in high density regions. It was found in these simulations (e.g., Hernquist et al. 1996) that most of the volume of the Universe at high redshift ($z \gtrsim 2$, see Davé et al. 1999 for the situation at later times) is filled with a warm (10^4 K), continuous, gaseous ionized medium. Fluctuations in this intergalactic medium (IGM) tend to have overdensities within a factor of 10 of the cosmic mean and resemble morphologically the filaments, walls and voids seen on larger scales in the galaxy distribution at lower redshifts. The dominant physical processes responsible for the state of this IGM and the Ly α absorption produced by it were anticipated by semi-analytic modelling of the Ly α forest (e.g., McGill 1990, Bi, Borner & Chu 1992). For completeness, we will summarize these processes below.

2.1 The Fluctuating Gunn-Peterson Approximation

The physical state of most of the volume of the baryonic IGM is governed by the photoionization heating of the UV radiation background, and the adiabatic cooling caused by the expansion of the Universe. The competition between these two processes drives gas elements towards a tight relation between temperature and density, so that

$$T = T_0 \rho_b^\alpha(\mathbf{x}), \quad (1)$$

where $\rho_b(\mathbf{x})$ is the density of baryonic gas in units of the cosmic mean. This relation holds well in simulations for $\rho_b \lesssim 10$ (see e.g., Katz, Weinberg & Hernquist 1996). Hui & Gnedin (1997) have explored the relation semi-analytically by considering the evolution of individual gas elements in the Zel'dovich Approximation. They find that the value of the parameters in equation (1) depend on the history of reionization and the spectral shape of the radiation background, and should lie in the narrow range $4000 \text{ K} \lesssim T_0 \lesssim 15,000 \text{ K}$ and $0.3 \lesssim \alpha \lesssim 0.6$.

The optical depth for Ly α absorption, τ is proportional to the density of neutral hydrogen (Gunn & Peterson 1965). In our case, this is equal to the gas density ρ_b multiplied by a recombination rate which is proportional to $\rho_b T^{-0.7}$. By using equation (1), we find that the optical depth is a power law function of the local density:

$$\tau(x) = A \rho_b(x)^\beta, \quad (2)$$

where x is a distance along one axis, taken to the line-of-sight towards the QSO (we are working in real-space for the moment). Because this result is simply a generalisation of Gunn-Peterson absorption for a non-uniform medium, it has been dubbed the Fluctuating Gunn-Peterson Approximation (FGPA, see Rauch et al. 1997, Croft et al. 1998a, Weinberg et al. 1998a). The FGPA amplitude, A , is dependent on cosmology and the state of the gas so that (e.g., Croft et al. 1999),

$$A = 0.835 \left(\frac{1+z}{4}\right)^6 \left(\frac{\Omega_b h^2}{0.02}\right)^2 \left(\frac{T_0}{10^4 \text{ K}}\right)^{-0.7} \times \left(\frac{h}{0.65}\right)^{-1} \left(\frac{H(z)/H_0}{4.46}\right)^{-1} \left(\frac{\Gamma}{10^{-12} \text{ s}^{-1}}\right)^{-1}. \quad (3)$$

Here Γ is the photoionization rate, $h = H_0/100 \text{ km s}^{-1} \text{ Mpc}^{-1}$, and Ω_b

is the ratio of the baryon density to the critical density. The FGPA slope, $\beta = 2 - 0.7\alpha \simeq 1.6$.

The FGPA has been tested in simulations (Croft et al. 1997, Weinberg 1999), and the predicted tight correlation found to hold well. The analysis in this paper will involve using equation (2) to relate the optical depth to the underlying real-space mass density. We will make predictions for the observable quantity, transmitted flux in a QSO spectrum, which we label ϕ :

$$\phi(x) = e^{-A\rho_b(x)^\beta}. \quad (4)$$

Equation (4) can be thought of as ‘‘local biasing relation’’ between the flux and mass distributions. It can be seen that in this relation, the only spatially varying quantity is $\rho_b(x)$ (ignoring global redshift evolution and assuming a smooth ionizing background). Given that the physical processes included in the derivation of the FGPA relation are the dominant ones, then the clustering properties of the Ly α forest should be determined mainly by the statistics of ρ_b . The emphasis in this paper is therefore on applying our knowledge of the behaviour of density perturbations to the Ly α forest. We will use analytical results for the non-linear evolution of density perturbations in an effort to understand the origin of the values of Ly α forest observables. The ultimate aim is that with this understanding, measurements made from observational data can be used to directly test both the gravitational instability hypothesis, and the picture of the Ly α forest outlined above, as well as throwing light on the nature of the primordial density fluctuations.

An alternative to the approach we adopt here would be to use the local relation Eq[4] to directly reconstruct the density field, rather than to predict its cumulants or the cumulants of the flux. This reconstructed field could then be used to estimate the statistical properties of the density (e.g., cumulants) in a straightforward way. This is not however simple to do in practice because of the saturation of flux in high density regions. Although large changes in high density regions have little effect on the statistics of the flux (i.e. the cumulants), they will totally change the statistics of the density. Any reconstruction technique will therefore have to deal with this missing information somehow. One approach for dealing with this problem has been presented by Nusser & Haehnelt (1998). In the present paper, we make use of the important fact that the power-law and exponential weighting of the density in the FGPA relation results in a flux distribution whose statistical properties are dominated by the small fluctuations, i.e. the linear or weakly non-linear regime.

2.2 Additional complications

There are a number of assumptions concerning the relationship between flux and mass which we should discuss before proceeding. First, the above equations apply to the density of gas, ρ_b rather than the total density of matter, ρ , which will be dominated by a dark matter component in the models we are considering. At the relatively low densities of interest here, the distribution of gas in simulations does however trace the dark matter well. Pressure forces on gas elements tend to be small compared to the gravitational forces, and non-hydrodynamical N-body simulations can be used to pro-

duce very similar spectra to the simulations which include these pressure effects (Weinberg et al. 1999). Simulations do have finite resolution limitations, though, and clustering in a dissipationless dark matter distribution with power extending to small scales cannot be followed with infinite resolution. The N-body only calculations so far used (e.g., Croft et al. 1998a) have a resolution comparable to the small scale smoothing produced by pressure effects. Hydrodynamical simulations at high resolution (e.g., Bryan et al. 1998) can be used to study this smoothing. In the case of analytic work, one can first consider the linear regime. In this case, the power spectrum of fluctuations in the gas density, $P_g(k)$ is a smoothed version of the dark matter power spectrum, $P_{DM}(k)$, so that

$$P_g(k) = \frac{P_{DM}(k)}{[1 + (k/k_j)^2]^2} \quad (5)$$

where k_j is the Jean’s wavenumber (see e.g., Peebles 1993). In tests of this result, Gnedin & Hui (1998) have shown that after reionization, the effective smoothing length is generally smaller, and modelling with a different (Gaussian) filter tends to give better results when compared with simulations. The situation in the non-linear regime will be more complicated. The Jeans length scales as $(\rho_b)^{-0.5}$, but due to the temperature density relation of equation 1, denser regions also tend to have higher temperatures, more thermal pressure, and more smoothing, so that the overall density dependence of the Jean’s length should be weak. Gnedin & Hui (1998) show that filtering the initial conditions of a dissipationless simulation with a single scale gives reasonable results compared to the full hydrodynamic case (although worse than their ‘‘Hydro-PM’’ technique, which involves adding a pressure term to the dissipationless simulation calculations). In our case, the analytic approximation for gravitational collapse which we use allows for filtering the evolved density with a top-hat filter in real-space (see the next sections and Appendix A1.2). It may be possible to vary the smoothing length as a function of density, but for reasons of simplicity we use a constant smoothing radius for now. Another possibility for the future might be self-consistent modelling of the hydrodynamic effects when following the evolution of density perturbations. This has been done numerically in 1D simulations of spherical collapse by Haiman et al. (1996).

Second, the FGPA itself will break down in regions of high density, because of shock heating of gas, collisional ionization, star formation, and other processes. We can quantify this by appealing to the results of hydrodynamic simulations. As stated above, the relation has been directly tested by Croft et al. (1997), who find that it works well at high redshifts, $z \gtrsim 2$, on a point by point basis, for $\rho_b \lesssim 10$. When we consider statistics that we might want to measure from the flux distribution, the situation is even better. For example, we can see using the numbers given for A above at $z = 3$ and equation (4), that optical depth will saturate ($\phi \lesssim 0.05$) for $\rho \gtrsim 3$. The physical processes occurring in regions with $\rho \gtrsim 3$ are therefore not likely to directly affect what we can measure. Of course, there will be indirect effects, for example, supernova winds may inhomogeneously heat the IGM out into lower density regions. Also, the reionization of HeII, which is expected to occur around $z \sim 3$, may cause inhomogeneous heating if it is patchy enough (Miralda-Escudé

and Rees 1994). Although we expect the volume occupied by regions which do follow the FGPA to be overwhelming in the high- z Universe, the statistical properties of the absorption predicted by analytical gravitational instability theory should be useful in testing the validity of this assumption. They should also help us decide if there is any appreciable contribution to clustering from spatial variations in the photoionization rate Γ , due to the inhomogeneity in the UV background. Any such variations are expected to be small in amplitude and to occur only on scales larger than we can probe directly at present (see e.g., Zuo 1992, Fardal & Shull 1993, Croft et al. 1999).

Third, we have so far only dealt with the density field in real-space, whereas measurements from QSO spectra are made in redshift-space. Both peculiar velocities and thermal broadening of absorption features should affect the statistics of ϕ to some degree. We will include both these effects in our predictions.

3 THE PROBABILITY DISTRIBUTION

We would like to make predictions for the one-point PDF of the flux ϕ and its moments. The one-point PDF of a given field ϕ is defined so that the probability of finding, at a random position x , a value $\phi(x)$ in the infinitesimal interval ϕ to $\phi + d\phi$, is $P(\phi)d\phi$.

To make these predictions we will first derive the corresponding probabilities $P(\rho)$, for the local matter overdensity $\rho = 1 + \delta$, where ρ is in units of the mean density $\rho(x) = n(x)/\langle n \rangle$. We will make indiscriminate use of either $\delta(x)$ or $\rho(x)$ as variables when describing density fluctuations. The second step is the assumption of a local relation with the form $\phi = f(\rho)$, (motivated by equation [4]). The PDF of the flux will then simply be obtained by performing a change of variables from the PDF of the density.

We start by assuming a (Gaussian) form for the PDF of the initial conditions, and then follow its evolution. As we will see, in our approach it is not necessary to assume Gaussian initial conditions, and this procedure can be extended to some other non-Gaussian models. We will do this with a model starting from χ^2 initial conditions in Section 6.1.

One important point to note about our predictions is that we are not creating artificial spectra but instead using an analytical model to evolve the density PDF and then predict the PDF of the flux directly. Our predictions for the density distribution will depend on only two parameters, equivalent to the slope and amplitude of the linear correlation function on the smoothing scale, γ , and σ_L^2 (see Sections 3, 4 and Appendix A1). This will allow us to cover a wide range of possibilities, and make predictions that are as generic as possible.

In this section we will also test the effects of varying the two parameters in the FGPA relation, A and β , which (equation [3]) contain information about the cosmic baryon density, ionizing background and reionization history of the Universe.

3.1 The PDF of the initial conditions

In the limit of early times, we assume a nearly homogeneous distribution with very small fluctuations (or seeds),

with given statistical properties. We will concentrate on the case where the statistics of the initial density are well described by Gaussian initial conditions, which correspond to a general class of models for the initial conditions. The one-point Gaussian probability distribution of an initial field δ is given by:

$$P_{IC}(\delta) = \frac{1}{\sqrt{2\pi\sigma_0^2}} \exp\left(-\frac{1}{2}\left[\frac{\delta}{\sigma_0}\right]^2\right) \quad (6)$$

As the overdensity must be positive, $\rho > 0$, we have that $\delta > -1$, and a Gaussian PDF only makes physical sense when the initial variance is small: $\sigma_0 \rightarrow 0$.

3.2 The evolved mass PDF

Because of gravitational growth, the evolution of δ will change the PDF from its initial form. For small fluctuations linear theory provides a simple way of predicting the time evolution of $\delta(t, x) = D(t)\delta_0(x)$, where $D(t)$ is the growth factor (equal to the scale factor $D = a$ for $\Omega = 1$), and $\delta_0(x)$ is the initial field. We will denote this linear prediction by δ_L . For Gaussian initial conditions the linear PDF is also Gaussian with a variance σ_L^2 , given by scaling the initial variance σ_0^2 by D^2 , so that $\sigma_L^2 = D^2\sigma_0^2$.

As mentioned in the introduction, there are a number of studies which predict the evolution of the PDF beyond linear theory. Here we will consider a generic class of local mappings along the lines introduced by Protogeris & Scherrer (1997). The idea is for us to relate the non-linear fluctuation $\delta(q)$ (in Lagrangian space) with the corresponding linear fluctuation $\delta_L(q) \equiv D\delta_0(q)$ using a universal (local) function. To simplify notation we choose to express this mapping as a relation between the non-linear overdensity $\rho = \delta + 1$ and the linear fluctuation δ_L , so that

$$\rho(q) = \mathcal{G}[\delta_L(q)]. \quad (7)$$

One such mapping is the spherical collapse model (SC) or shear-free approximation. For Gaussian IC, the SC approximation happens to give the exact statistical properties of the density (cumulants of arbitrary order) at leading order in perturbation theory (as found by Bernardeau 1992 in the context of the cumulant generating function), and provides a very good approximation to higher orders (see FG98). Physically, this mapping corresponds to taking the limit where shear is neglected. In this case the equations for the growth of δ , in Lagrangian space, are identical to those given by spherical collapse. So, in the perturbative regime, the SC is the best mapping possible, given the local assumption made in equation (7). The local transformation naturally occurs in Lagrangian space q (comoving with the initial fluid element). The important point to notice here is that although the local mapping is not the exact solution to the evolution of δ (which is in general non-local), it does give the correct clustering properties in the weakly non-linear regime. In the Appendix we give some specific examples for the transformation \mathcal{G} .

The one-point PDF induced by the above transformation, in terms of the initial one-point PDF P_{IC} , is

$$P_L(\rho) = P_{IC}(\delta_L) \left| \frac{d\delta_L}{d\rho} \right|, \quad (8)$$

where $\delta_L = \mathcal{G}^{-1}[\rho]$. As mentioned before, the above expression corresponds to the probability distribution of the evolved field in Lagrangian space, q . To relate Lagrangian and Eulerian probabilities we use the law of mass conservation: $d\delta(q) = \rho d\delta(x)$, where $\rho(x) = 1 + \delta(x)$ is the overdensity in Eulerian coordinates. We therefore have

$$P(\rho) = \frac{1}{N} \frac{P_{IC}(\delta_L)}{\rho} \left| \frac{d\delta_L}{d\rho} \right|, \quad (9)$$

where N is a normalization constant. We will show some of these predictions in Section 5 (e.g., Fig. 7).

3.3 The PDF of the flux

We next assume a local transformation which relates the underlying smoothed overdensity to some observable quantity ϕ :

$$\phi = f(\rho) \quad (10)$$

This quantity can further be related to the linear density field, so that

$$\phi = f[\mathcal{G}(\delta_L)]. \quad (11)$$

The PDF of ϕ will then related to that of the density by a simple change of variable:

$$P(\phi) = P(\rho) \left| \frac{d\rho}{d\phi} \right| = \frac{1}{N} \frac{P_{IC}(\delta_L)}{\rho} \left| \frac{d\delta_L}{d\phi} \right|, \quad (12)$$

where $\delta_L = \mathcal{G}^{-1}[f^{-1}[\phi]]$ and $\rho = f^{-1}[\phi]$. Thus, given the transformations f and \mathcal{G} , the above equations provide us with analytical (or maybe numerical) expressions for the PDF of ϕ .

In the present work, we concentrate on the cumulants (see Section 5.3 for a definition) of the flux, rather than the PDF itself. The reason for this is that, given the local assumption, the cumulants are more accurately determined (see Section 5.3 for more details). Nevertheless, we will see in Section 5 that the above prediction gives a good qualitative description of the PDF (see e.g., Fig. 8).

3.4 Redshift-space distortions

The smoothed flux and its corresponding optical depth $\tau = -\ln \phi$ has been assumed to be a local function of the smoothed non-linear density ρ . The optical depth τ at a given real-space position along the line of sight r will lie at a redshift-space position s in a QSO spectrum:

$$s = r + v_r/H, \quad (13)$$

where v_r is the component of the smoothed peculiar velocity along the line of sight at r . Note that the redshift distortion is of the smoothed field, where the smoothing, due to finite gas pressure, occurs in real-space. The redshift mapping will conserve optical depth, $\tau_s ds = \tau dr$, so that we have:

$$\tau_s = \tau \left| \frac{dr}{ds} \right| = \tau \left| 1 + \frac{1}{H} \frac{dv_r}{dr} \right|^{-1}. \quad (14)$$

In general, the relation between dv_r/dr and ρ will be complex. However, in the SC model, spherical symmetry leads to a great simplification:

$$\frac{dv_r}{dr} = \frac{1}{3} \nabla \cdot v \equiv \frac{H}{3} \theta, \quad (15)$$

as, by symmetry, derivatives are the same in all directions (this idea has also been used by FG98 and by Scherrer & Gaztañaga 1998). We can now again use the local mapping to relate velocity divergence to the linear field: $\theta = \mathcal{G}_v[\delta_L]$, as in equation (A7). Thus we have that the redshift optical depth is given by a different mapping:

$$\tau_s(\rho) = \tau(\rho) \left| 1 + \frac{1}{3} \theta(\rho) \right|^{-1}. \quad (16)$$

The redshift-space flux is simply:

$$\phi_s = \exp[-\tau_s(\rho)], \quad (17)$$

and its PDF can be computed with a simple change of variables:

$$P(\phi_s) = \frac{1}{N} \frac{P_{IC}(\delta_L)}{\rho} \left| \frac{d\delta_L}{d\phi_s} \right|. \quad (18)$$

4 THE CUMULANTS

4.1 Definitions

Consider a generic field, ϕ , which could be either the measured flux in a 1D spectrum, $\phi = \phi(\rho)$, or the mass density in 3D space $\phi = \rho$. The J th-order (one-point) moments of this field are defined by (note the subscript ‘‘c’’ for connected):

$$m_J = \langle \phi^J \rangle = \int P(\phi) \phi^J d\phi. \quad (19)$$

Given the above relations we can choose to calculate the moments by integrating over δ_L :

$$m_J = \int d\delta_L \frac{P_{IC}[\delta_L]}{\rho(\delta_L)} \phi^J(\rho(\delta_L)), \quad (20)$$

or over the non-linear overdensity ρ :

$$m_J = \int d\rho \frac{P_{IC}[\delta_L(\rho)]}{\rho} \left| \frac{d\delta_L}{d\rho} \right| \phi^J(\rho). \quad (21)$$

Here ϕ can refer either to real-space fields or fields which have been distorted into redshift-space (e.g., equation [17]). The J th order *reduced* one-point moments, or cumulants k_J , of the field ϕ are defined by:

$$k_J \equiv \langle \phi^J \rangle_c = \left. \frac{\partial \log M(t)}{\partial t} \right|_{t \rightarrow 0}, \quad (22)$$

where $M(t) = \langle \exp(\phi t) \rangle$ is the generating functional of the (unreduced) moments:

$$m_J \equiv \langle \phi^J \rangle = \left. \frac{\partial M(t)}{\partial t} \right|_{t \rightarrow 0}. \quad (23)$$

The first reduced moments are:

$$\begin{aligned} k_1 &= m_1 \\ k_2 &= m_2 - m_1^2 \\ k_3 &= m_3 - 3m_1 m_2 + 2m_1^3 \\ k_4 &= m_4 - 6m_1^4 + 12m_1^2 m_2 - 3m_2^2 - 4m_1 m_3 \end{aligned} \quad (24)$$

and so on. Note that even when we normalise the flux so that the mean is zero ($m_1 = 0$), the cumulants are different from the central moments in that the lower order moments

have been subtracted from them, so that $k_4 = m_4 - 3m_2^2$ for $m_1 = 0$.

It is interesting to define the following one-point hierarchical constants:

$$S_J = \frac{k_J}{k_2^{J-1}} \quad J > 2 \quad (25)$$

These quantities turn out to be roughly constant under gravitational evolution from Gaussian initial conditions (see e.g., Gaztañaga & Baugh 1995 and references therein).

4.2 Fully non-linear predictions

We now use the one-point flux PDF obtained from equation (12) to predict the one-point moments of the flux. As mentioned in Section 3, to make the predictions we need the value of the linear variance σ_L^2 , and the local relation equation (7), which only depends on the smoothing slope γ (see equation A17 for the definition of γ). For non-linear mapping relations, we try each of the two cases introduced in the Appendix. In the following figures we will only plot results for the Spherical Collapse (SC) mapping because they coincide perfectly with the results for the Generalized Zel'dovich Approximation (GZA) model in equation (A10) with $\alpha = 21/13$.

We are interested primarily in the evolution of the density PDF and the weighting which the FGPA relation gives to the clustering properties of the density field. In order to separate the effects of redshift distortions from those of density evolution, we will present results in real-space first.

4.2.1 The mean flux

Figure 1 shows the mean flux $\langle \phi \rangle$ ($= m_1$ in equation [19]) as a function of σ_L^2 for several values of A , β (the parameters in the FGPA relation) and γ .

For small σ_L all predictions tend to $\langle \phi \rangle = \exp(-A)$ which corresponds to the flux at the mean overdensity: $\phi \rightarrow \exp(-A)$ as $\rho \rightarrow 1$. We will see in next subsection that this is the leading order PT prediction. For larger σ_L the mean flux becomes larger, as expected, but it is flatter as a function of σ_L^2 when there is less smoothing, i.e., when γ is less negative. Less smoothing of the density will correspond to larger non-linearities, at least in PT (see e.g., FG98). This seems to indicate that the effect of non-linearities is to *reduce* the mean flux, competing with linear growth, which *increases* the mean flux.

4.2.2 The variance of the flux

We define the variance using the normalized flux:

$$\sigma_\phi^2 = \left\langle \left(\frac{\phi - \langle \phi \rangle}{\langle \phi \rangle} \right)^2 \right\rangle_c. \quad (26)$$

The overall normalization by $\langle \phi \rangle$ is a convention, in analogy to what is done for density fluctuations. Figure 2 shows the predicted variance σ_ϕ^2 as a function of σ_L^2 for several values of A , β and γ . For small σ_L^2 these results reproduce the linear relation: $\sigma_\phi^2 = b_1^2 \sigma_L^2$ (see equation [32]). Deviation from this power-law relation (of index 1) occurs as σ_L^2 is increased, and occurs sooner for larger values of A and β . For $\gamma > 0$,

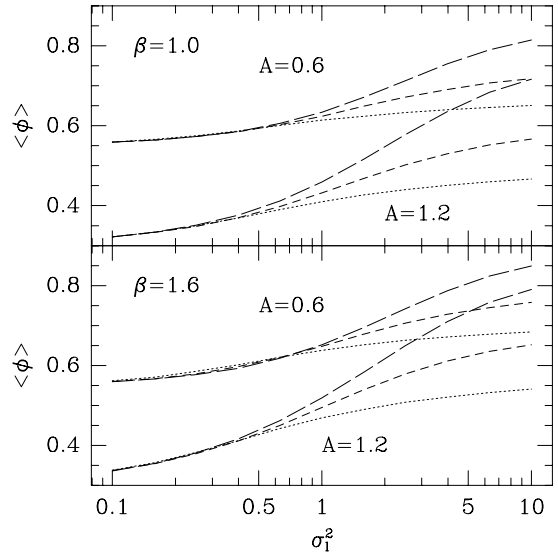


Figure 1. Mean flux $\langle \phi \rangle$ as a function of the linear variance σ_L^2 for different values of A and β . The dotted, short-dashed and long-dashed lines show the predictions for $\gamma = 0, -1$ and -2 respectively.

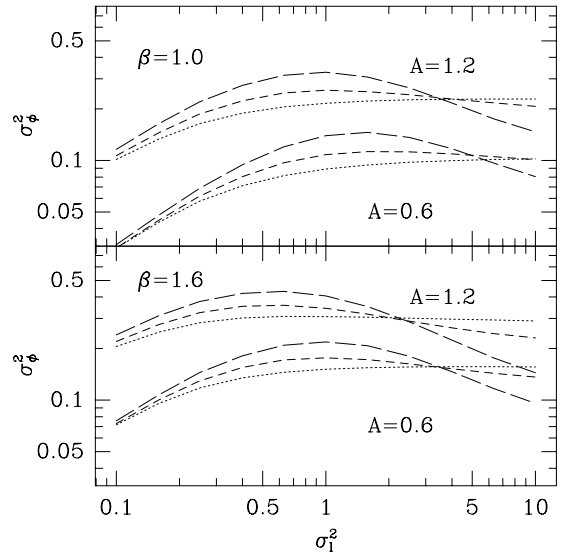


Figure 2. The variance of the flux σ_ϕ^2 as a function of σ_L^2 . The meaning of the line types is the same as in Figure 1.

when σ_L^2 reaches ~ 1 , σ_ϕ^2 seems to reach a maximum and then decreases again like a power-law for large σ_L^2 .

We can again see that the predictions become flatter as a function of σ_L^2 when there is less smoothing, i.e., for less negative γ .

4.2.3 The skewness of the flux

In a similar way, we define the (normalized hierarchical) skewness of the flux as:

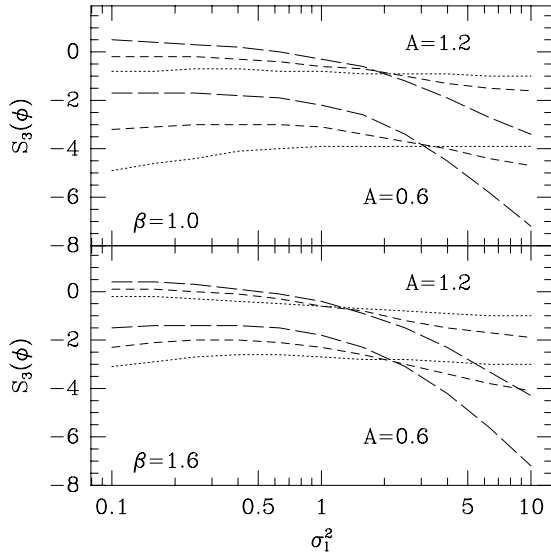


Figure 3. The Hierarchical skewness of the flux, $S_3(\phi)$, as a function of σ_L^2 . The meaning of the line types is the same as in Figure 1.

$$S_3(\phi) = \frac{\langle (\phi / \langle \phi \rangle - 1)^3 \rangle_c}{\sigma_\phi^4}. \quad (27)$$

Figure 3 shows the predicted skewness, as a function of σ_L^2 for several values of A , β and γ . Because of the dependence of flux on density in the FGPA relation (more density, less flux), while the density distribution is positively skewed, the skewness of the flux tends to be negative for most values of the parameters.

For small σ_L^2 the results tend to a constant as expected in leading order PT (see equation [32]). We will examine the PT relations in more detail in Section 4.3. For the moment, we note that there again seems to be less variation in $S_3(\phi)$ as a function of σ_L^2 for cases with less smoothing (less negative γ).

4.2.4 The kurtosis of the flux

The (normalized hierarchical) kurtosis of the flux is defined in a similar fashion:

$$S_4(\phi) = \frac{\langle (\phi / \langle \phi \rangle - 1)^4 \rangle_c}{\sigma_\phi^6}. \quad (28)$$

Figure 4 shows the predicted kurtosis, as a function of σ_L^2 for several values of β and γ . For clarity we only show one value of A .

For small σ_L^2 these results tend to the constant value predicted by leading order PT (see equation [32]). Being a fourth moment, $S_4\phi$ is extremely sensitive to deviations from Gaussianity which occur as the density field evolves and σ_L^2 increases. This sensitivity seems to be larger for lower values of β , presumably because when β is high, high density parts of the PDF which might contribute heavily to the kurtosis of the density field have little weight in the statistics in ϕ .

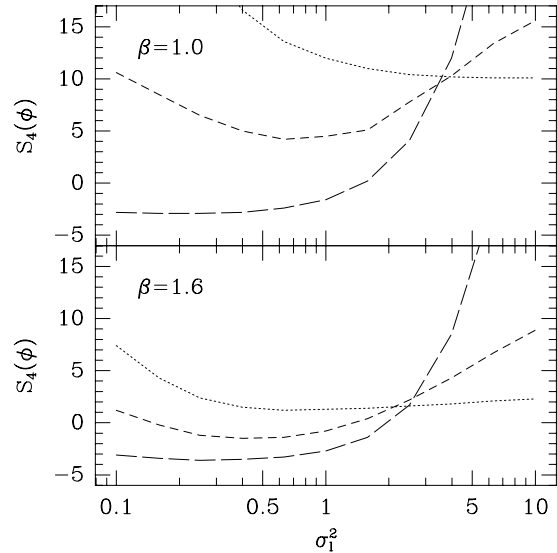


Figure 4. Same as Figure 2 for the Hierarchical kurtosis. For clarity only $A = 0.6$ is shown.

4.3 Perturbative predictions

An alternative to using the PDF is to calculate the cumulants directly from the perturbative expansion along the lines suggested (in the context of galaxy biasing) by Fry & Gaztañaga (1993). That is we take:

$$\begin{aligned} \phi &= e^{-A\rho^\beta} = b_1 \sum_{k=0} \frac{c_k}{k!} \delta^k \\ b_1 &= -A\beta e^{-A} \\ c_0 &= -\frac{1}{A\beta} \\ c_1 &= 1 \\ c_2 &= -1 + \beta - A\beta \\ c_3 &= 2 - 3\beta + \beta^2 + 3A\beta - 3A\beta^2 + A^2\beta^2 \end{aligned} \quad (29)$$

(30)

and so on. From this expansion one can simply estimate the moments by taking mean values to the powers of ϕ . The leading order terms in σ_L^2 are:

$$\begin{aligned} \langle \phi \rangle &= e^{-A} \\ \sigma_\phi^2 &= b_1^2 \sigma_L^2 \\ S_3(\phi) &= \frac{S_3 + 3c_2}{b_1} \\ S_4(\phi) &= \frac{S_4 + 12S_3c_2 + 12c_2^2 + 4c_3}{b_1^2}, \end{aligned} \quad (31)$$

(32)

where S_3 and S_4 are the leading order (hierarchical) skewness and kurtosis for the density field. For Gaussian initial conditions they are: $S_3 = 34/7 + \gamma$ and $S_4 = 60712/1323 + 62/3\gamma + 7/3\gamma^2$ (both in the SC model and PT theory). For non-Gaussian initial conditions, one would have to add the initial contribution, e.g., $S_3 = S_3^0 + 34/7 + \gamma$.

These predictions are shown as a straight continuous

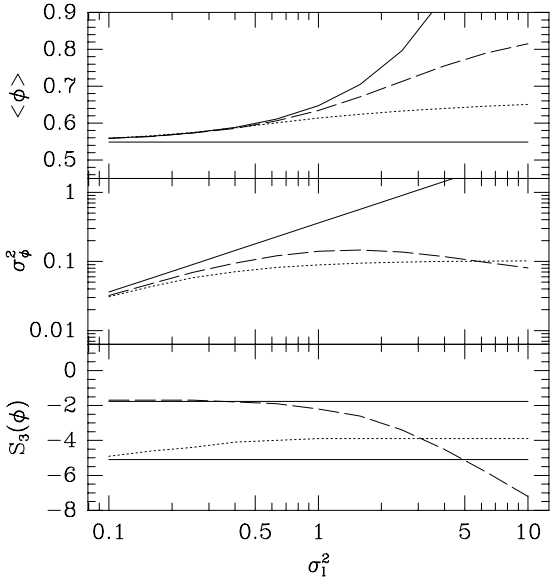


Figure 5. Perturbative predictions for the one-point flux moments compared to the fully non-linear predictions. Mean flux $\langle\phi\rangle$ (top), variance σ_ϕ^2 (middle panel) and skewness $S_3(\phi)$ (bottom) are shown as a function of the linear variance σ_L^2 for $A = 0.6$ and $\beta = 1.0$. The dotted and long-dashed lines show the non-linear predictions (Section 4.2) for $\gamma = 0$ and $\gamma = -2$ smoothing respectively. The straight continuous lines show the corresponding leading order perturbative prediction (Section 4.3), valid for $\sigma_L \rightarrow 0$. The solid curve in the top panel is the perturbative prediction for $\langle\phi\rangle$ including the effect of a higher order (loop) correction (see equation [33]).

lines in Figure 5, where they are compared to the full (non-perturbative) calculation in the SC model for two values of the smoothing slope, $\gamma = 0$ (long-dashed line) and $\gamma = -2$ (dotted line). We can see that the expressions only converge on the correct result asymptotically as $\sigma_L \rightarrow 0$. The relative performance depends on γ , with steeper slopes giving better results. It is easy to calculate higher order (loop) corrections (see e.g., FG98). For example:

$$\langle\phi\rangle = e^{-a} \left[1 + \frac{A\beta}{2}(1 - \beta + A\beta)\sigma_L^2 + \mathcal{O}(\sigma_L^4) \right], \quad (33)$$

This prediction for the mean flux is shown as a curved continuous line in the top panel of Figure 5, and seem to work up to scales where $\sigma_L \simeq 1$. We find however that the agreement becomes worse for larger values of A and β . A similar tendency is found for other moments.

We have seen that even when high-order corrections are included, this perturbative approach only works well for small values of σ_L , A and β . It is likely to have only a limited applicability when we consider the situation in the observed Universe, where typical values of $\sigma_L \geq 1$ are expected, (at least for redshifts $z \lesssim 4$). Given that we have the possibility of implementing the SC model (or the GZA model) to arbitrary order, one could ask why we bother with a perturbative approach. The first obvious reason is that it gives us compact analytical predictions, simple formulae which are functions of the input variables (A , β , γ and σ_L^2). A second reason is that by using this approach, it may be possible to introduce the PT solutions. As mentioned before, PT only

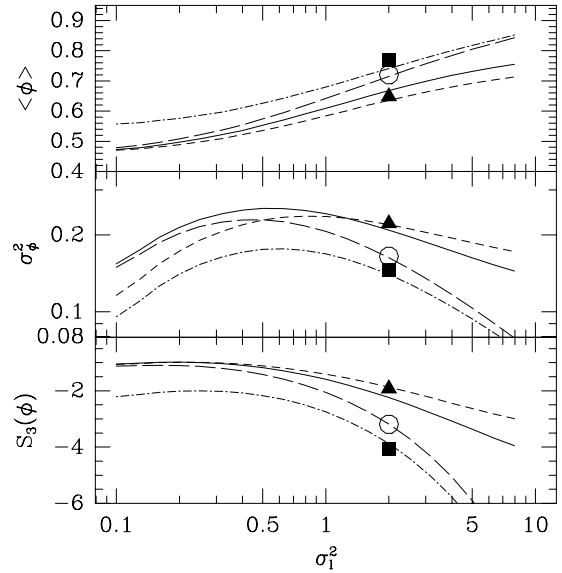


Figure 6. The effect of redshift-space distortions on the one-point moments. Mean flux $\langle\phi\rangle$ (top), variance σ_ϕ^2 and skewness $S_3(\phi)$ (bottom) are plotted as a function of the linear variance σ_L^2 for $\gamma = 1$, $A = 0.8$ and $\beta = 1.6$. The short-dashed and continuous lines show the predictions in real and redshift-space (peculiar velocities only) respectively. The long-dashed lines correspond to predictions in redshift-space with an additional velocity dispersion component on small scales (added in order to match simulation results - see text). The dot-dashed lines show the predictions in redshift-space with thermal broadening as well as peculiar velocities (and the extra small-scale dispersion). In modelling the thermal broadening component to the redshift distortion we have assumed that the temperature depends on the density, as predicted by equation (1) (see Section 4.4). The points show results from simulated spectra (set [a]) described in Section 5. The triangles, circles and squares represent spectra in real space, redshift-space with no thermal broadening, and redshift-space with thermal-broadening, respectively.

differs from the SC model through the shear contributions, and although these are typically small (as will be shown) they might still be relevant for higher precision comparisons. It is not clear nevertheless than one could obtain higher accuracy at $\sigma_L \gtrsim 1$, given the limitations of a perturbative approach (i.e., convergence of the series).

4.4 Predictions in redshift-space

We now turn to the more observationally realistic case where redshift distortions are included. Fig. 6 shows how the (fully non-linear) predictions change when given in redshift-space. We use the formalism of Section 3.4 (e.g., equation [17]), results which allow one to estimate the effects of peculiar velocity distortions. The redshift distortions caused by thermal broadening can be treated in a similar way, and we will also do this below. For clarity we only show a single value of A , β and γ , but similar effects are found if we use other values. We have also plotted some simulation points on Fig. 6. The simulations will be described fully in the next section. For the moment, it is only necessary to mention here that, for purposes of comparison, the simulation density PDFs

can be described by the two parameters, γ and σ_L^2 (evaluated from the power spectrum of initial fluctuations used to set up the simulation). The transformation from density into flux in the simulations has also been carried out using the FGPA relation. We plot points both with and without including redshift distortions from peculiar motions and thermal broadening.

If we concentrate on the mean flux first, and ignore thermal broadening, we can see that $\langle\phi\rangle$ in redshift-space (continuous line in the top panel) seems to converge to same value as the real-space mean flux (short-dashed line) for small σ_L . For $\sigma_L \gtrsim 1$ the mean flux is larger in redshift-space.

The variance in the flux, σ_ϕ^2 , defined by equation (26) is shown in the middle panel of Fig. 6. We can see that this quantity is larger in redshift-space than in real-space for $\sigma_L \lesssim 1$, a trend that is reversed for $\sigma_L \gtrsim 1$. The former is presumably due to the same ‘‘squashing effect’’ that is seen in studies of the density field, where infall of matter into high density regions enhances clustering (Kaiser 1987). The latter effect can be attributed to a relative decrease in the level of redshift-space clustering caused by high velocity dispersion along the line of sight.

The skewness, defined by equation (27) is shown in the bottom panel of Fig. 6. For small σ_L , the redshift-space (continuous line) $S_3(\phi)$ seems to match the real-space value (dashed line). For $\sigma_L \gtrsim 1$, $S_3(\phi)$ is smaller in redshift-space.

The simulation points on the plot in real space (triangle) agree with predictions in the real space. In redshift-space (open circles), although the sign of the change caused by the peculiar velocity distortions is correct, the predictions do not agree in detail. Our interpretation of this is that the SC model does not predict enough random non-linear velocity dispersion. We have therefore added a velocity dispersion by hand, by adding in a velocity divergence term, θ_{disp} to equation (17):

$$\tau_s(\rho) = \tau(\rho) \left| 1 + \frac{1}{3} [\theta(\rho) + \theta_{\text{disp}}(\sigma_L^2)] \right|^{-1}. \quad (34)$$

In order that the asymptotic behaviour of θ_{disp} be satisfied (non-linear dispersion $\rightarrow 0$ as $\sigma_L^2 \rightarrow 0$), we have adopted the functional form $\theta_{\text{disp}} = C\sigma_L^2$. Predictions from the SC model including the effect of this term are shown in fig. 6 as a long dashed line. We have adjusted the constant C so that the predictions go through the simulation point in redshift-space.

Next, we include thermal broadening in our predictions. For the moderate optical depths we are concerned with here, the relevant Voigt profile can well be approximated by a Gaussian velocity dispersion. The width of this Gaussian profile, $\sigma_T \simeq \sigma_{T_0}(T/T_0)^{1/2}$, where $\sigma_{T_0} \simeq 13/\sqrt{2}$ km s $^{-1}$ for $T_0 \simeq 10^4$ K. From equation (1) we have $T \propto \rho^{0.6}$, so that $\sigma_T \simeq \sigma_{T_0}\rho^{0.3}$. We can think of thermal broadening as resulting in the addition of a thermal velocity component, θ_T , to the divergence field θ in equation (16). We will model this thermal component in a similar way to the extra non-linear dispersion term (θ_{disp}) defined above, which can be thought of as a ‘‘turbulent’’ broadening term. We simply model the additional thermal dispersion using its rms value, so that,

$$\theta_T(\rho) \simeq 3 \frac{\sigma_T}{H\Delta} \simeq \frac{\sigma_{T_0}}{H\Delta} \rho^{0.3}, \quad (35)$$

where Δ is distance in the QSO spectrum which corresponds

to the scale of Jean’s smoothing. This density-dependent term then enters the RHS of equation (34), alongside θ_{disp} . The long-dashed line in Fig. 6 shows the effect of thermal broadening using this prescription. We have used the value σ_{T_0} appropriate to the simulation (see Section 5.2 for details), whose thermally broadened results are plotted as a solid square. As can be seen, thermal broadening results in more flux being absorbed, and yields a lower value of σ_ϕ^2 . This is as we should expect, given that the distribution of optical depth has effectively been smoothed out by the addition of a dispersion.

It is evident from these results that the one-point moments depend fairly strongly on the details of redshift distortion modelling, which are likely to be poorly constrained a priori in our approximate treatment. Fortunately, much of the uncertainty can be removed by setting the mean flux, $\langle\phi\rangle$, to be equal to some (observed) value. We will show later (Section 5.5) that by doing this, the moments can be made insensitive to the inclusion of redshift distortions.

5 COMPARISON TO SIMULATIONS

As the emphasis of this paper is on the role of gravitational evolution of the density field, we now test the analytic techniques we have employed against numerical simulations of gravitational clustering. The N-body only simulations which we use do not allow us to perform tests of the validity of the model we have assumed for relating the mass distribution to an optical depth distribution (the FGPA, Section 2). Any difference between the statistical properties of the Ly α forest we predict and those observed in nature could therefore stem from a misapplication of the FGPA, rather than from problems with the underlying density field. Tests performed in other contexts show that this is unlikely, as a dissipationless approach to simulating the Ly α forest can perform well (see e.g. Croft et al. 1998a, Weinberg et al. 1999) in comparison with the full hydrodynamic case. Approximate methods should nevertheless be tested on a case by case basis, and we reserve comparisons with hydrodynamic simulations for future work.

5.1 Simulations

The simulations we use have all been run with a P 3 M N-body code (Efstathiou & Eastwood 1981, Efstathiou et al. 1985). The softening length of the PP interaction was made large (1 mesh cell), for simulation sets (a-c) because high spatial resolution is not needed. We have not attempted to simulate any particular favoured cosmological models or even to make sure that cases are likely to be compatible with expectations for the nature of the density field at high redshift. We are more interested in spanning a wide range of values of σ_L^2 , and γ , the parameters which determine the nature of the evolved density field in the SC model. To this end, we use outputs from three different sets of simulations. The initial conditions for all runs were Gaussian random fields with CDM-type power spectra of the form specified by Efstathiou, Bond & White (1992), with a shape parameter Γ , so that

$$P(k) \propto \frac{k}{[1 + (ak + (bk)^{3/2} + (ck)^2)^\nu]^{2/\nu}} \quad (36)$$

where $\nu = 1.13$, $a = 6.4/\Gamma h^{-1}\text{Mpc}$, $b = 3.0/\Gamma h^{-1}\text{Mpc}$, $c = 1.7/\Gamma h^{-1}\text{Mpc}$. There are five realizations with different random phases in each set of simulations, which are described below.

(a) A set with a box-size $40 h^{-1}\text{Mpc}$ and shape parameter $\Gamma = 0.5$. The model was run to $z = 3$ with an Einstein-de-Sitter cosmology. At that redshift $\sigma_L^2 = 2.0$, at the smoothing radius (see below), which was $0.31 h^{-1}\text{Mpc}$ (comoving). The linear slope at the smoothing scale, $\gamma = -0.8$. These simulations were run with 200^3 particles and 256^3 cells.

(b) A set with box size $22.22 h^{-1}\text{Mpc}$, 128^3 particles, $\Gamma = 0.5$, and an Einstein-de-Sitter cosmology. Simulated spectra were made from this set assuming that $z = 3$, but several different outputs were used with varying amplitudes of mass fluctuations. The smoothing radius was $0.31 h^{-1}\text{Mpc}$ (comoving), on which scale the linear slope was $\gamma = -0.8$. The value of σ_L^2 on this scale ranged from 0.02 to 7.5 for the different outputs.

(c) A set the same as (b), except with $\Gamma = 10$. The smoothing radius was again $0.31 h^{-1}\text{Mpc}$ (comoving), on which scale the linear slope was $\gamma = -1.8$. The value of σ_L^2 on this scale ranged from 0.03 to 10 for the different outputs.

(d) A set with box size $20 h^{-1}\text{Mpc}$, 126^3 , particles and $\Gamma = 3.8$. This set was originally used as ensemble G in Baugh, Gaztañaga & Efstathiou 1995, but the box size was taken to be larger, and hence Γ was lower. The smoothing scale is $0.37 h^{-1}\text{Mpc}$, where $\gamma \simeq -1.5$, and $\sigma_L^2 = 0.25$ (at $z = 3$). The cosmology assumed has $\Omega = 0.2$ and $\Omega_\Lambda = 0.8$ at $z = 0$.

We have also run a single simulation with the same parameters as those in set (a), except with a box of size $11.11 h^{-1}\text{Mpc}$, and 128^3 particles, so that the mass resolution is increased by a factor of ~ 12 .

5.2 Simulated spectra

To make simulated spectra from the N-body outputs, we use the following procedure (see also Hui, Gnedin & Zhang 1997, Croft et al. 1998a). The particle density and momentum distribution is assigned to a (256^3) grid using a TSC (triangular shaped clouds, Hockney & Eastwood 1981) scheme. The resulting fields are smoothed in Fourier space with a filter, which in our case is a top-hat with radius given in Section 5.1 above. We also use a very narrow Gaussian filter (with σ 0.1 times the top-hat radius) in order to ensure that density is non-zero everywhere. The velocity fields are computed by dividing the momentum by the density everywhere. Spectra are selected as lines-of-sight through the box, parallel to one of the axes (we select the axis randomly for each line-of-sight). These one-dimensional density fields are then converted to an optical depth distribution using equation (2). We also compute the temperature distribution of the gas using equation (1), with $\alpha = 0.6$ and $T_0 = 10^4\text{K}$. The optical depths are then converted from real-space to redshift-space by convolution with the line-of-sight velocity field and with a Gaussian filter with the appropriate thermal broadening width.

We estimate the one-point statistics of the flux in the spectra without any additional smoothing using counts-in-cells and the estimators of Section 4.2. We extract 5000 spectra from each simulation realization and estimate statistical errors from the scatter in results between the 5 realizations.

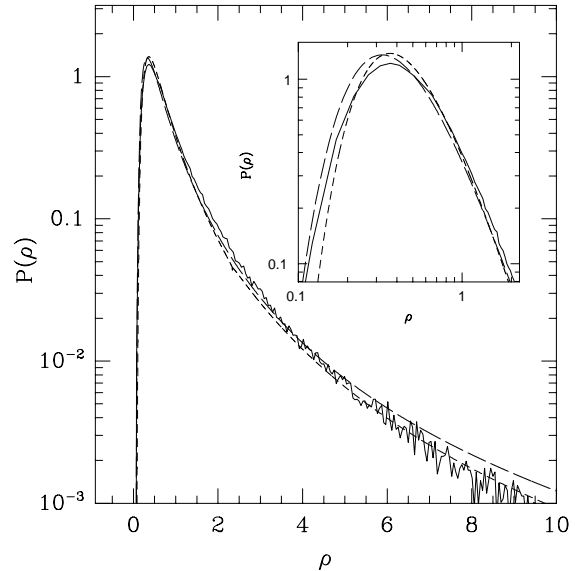


Figure 7. The one-point PDF of the density field ρ measured from N-body simulations (continuous line, set [a], see Section 5.1). The simulation density field was smoothed with top-hat cell on a scale with linear variance $\sigma_L^2 \simeq 2$ and slope $\gamma = -1$. The prediction of two approximations to PT are also shown: the Spherical Collapse model (short-dashed line) and the GZA in $\alpha = 21/13$ dimensions (long-dashed line).

We find that the resulting error bars are typically much smaller than the symbol size and so we do not plot them in the figures. Small systematic errors will arise because of the additional smoothing involved in using a mass assignment scheme, also because of shot noise from particle discreteness.

5.3 The PDF of density and flux

We first compare the PDF of the density in the simulations with the analytical predictions, both in real space. The one-point density PDF estimated from simulation lines-of-sight (using simulation set [a]) is shown in Fig. 7 as a continuous line. The analytical predictions are shown as a short-dashed (SC) and long-dashed (GZA) line. In evaluating the predictions we have used $\gamma \simeq -1$ and $\sigma_L^2 \simeq 2$ which correspond to the appropriate linear theory values for simulation set (a).

Note that the spherical collapse model is only an approximation to PT, so we do not expect to recover the PDF exactly, even close to $\delta \simeq 0$. To carry out the exact recovery we would have to include non-local (tidal) effects. The mean tidal effects vary in proportion to the linear variance and the leading contribution (when variance goes to zero) is only local (but non-linear). Tidal effects seem to distort the PDF, turning some $\delta = 0$ fluctuations into either voids $\delta \simeq -\sigma$ or overdensities $\delta \simeq \sigma$, so that the real peak in the PDF is slightly lower than SC or GZA. This distortion is significant, given that the statistical errors on the simulation result are small. The overall shape is however similar, as we can see from Fig. 7. The lower order moments of the density are also fairly similar: tidal effects tend to cancel out. When the variance is small (and the PDF tends to a Gaussian), the PDF can be defined one-to-one by its moments (e.g., with

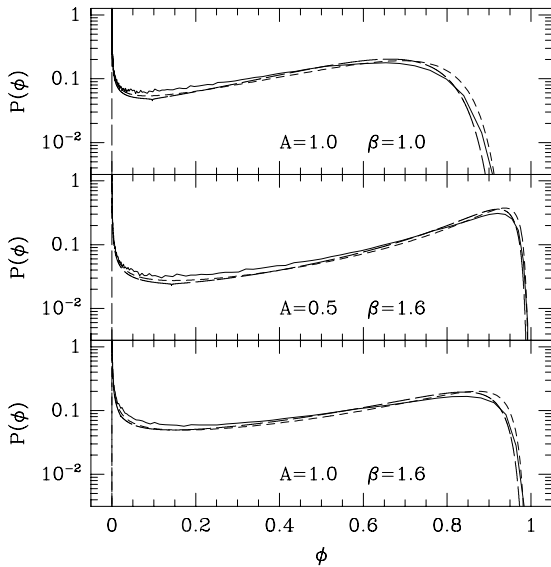


Figure 8. PDF of the flux evaluated using the same density distribution plotted in Fig. 7. Three different values of the FGPA parameters A and β are used as shown in each panel. The one-point PDF in the simulations is shown as continuous lines and is compared with the predictions of the two PT approximations, the Spherical Collapse model (short-dashed line), and the GZA in $\alpha = 21/13$ dimensions (long-dashed line). All results are in real-space.

an Edgeworth expansion). In this limit tidal effects vanish and both the PDF and the moments are given exactly by the SC model.

Thus, for the density distribution, the statistics of the moments are dominated by the contribution of local dynamics to the PDF and tidal effects are subdominant (they tend to cancel out when taking the mean). It is plausible that a similar sort of cancellation will happen for the statistics of the flux. In the next sections, we will therefore concentrate on predictions for the moments of the flux.

Different density regimes will be prominent if we consider the PDF of the flux, as it is a transformed version of the density PDF. In Fig. 8 we apply the FGPA relation (equation 4) in real-space to the density PDF from Fig. 7. The resulting flux distributions are rather flat, with the high density tail being confined to a small region of flux space near $\phi = 0$. Varying the parameters A and β produces most notable differences in the fraction of spectra which show little absorption. We can see that the lower β is, the less likely it is that any pixels will be seen with values near the unabsorbed QSO flux. The specific case with $\beta = 1.0$ is not realistic, though, as β is expected to be $\gtrsim 1.6$ for all reasonable reionization histories (Hui & Gnedin 1997).

In Fig. 9 we show the effect of redshift distortions on the flux PDF. We have used the prescription of Section 4.4 for making the predictions, including thermal broadening. The effect of the distortions is to evacuate the low density regions, as we might expect. The effect is very noticeable, as the peak of the PDF is raised substantially. Note that to make this plot, we have not added an additional small scale velocity dispersion, as we did previously to obtain a

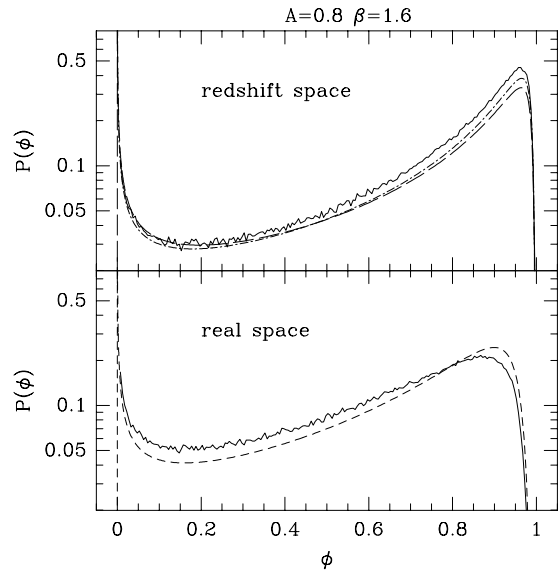


Figure 9. PDF of the flux evaluated from the same density distribution used in Fig. 7 (simulation set [a]). The one-point PDF in the simulations is shown as a solid line. Real-space results are plotted in the bottom panel, and results in redshift-space with thermal broadening in the top panel. These results are compared with the appropriate analytical predictions, using the Spherical Collapse model (short-dashed line) and the GZA in $\alpha = 21/13$ dimensions (long-dashed line).

closer match to the one-point moments in simulations (Fig. 6). We can see that the agreement of the predictions and simulations for the PDF in Figure 9 is still good, showing that our redshift modelling is at least a good qualitative approximation to the underlying physical processes.

5.4 Cumulants of the flux

In Fig. 10 we compare predictions and simulation results (for simulation sets [a] and [d]) for the mean flux $\langle \phi \rangle$, the variance σ_ϕ^2 , skewness $S_3(\phi)$ and kurtosis $S_4(\phi)$. In all cases we have used $\beta = 1.6$, and we show the moments as a function of the value of A . All results in this fig. have been evaluated in real-space. Squares correspond to simulation set (a), in which the one-point linear variance of the density field, $\sigma_L^2 = 2$ (the non-linear value is $\sigma^2 \simeq 4$) and the linear slope on the smoothing scale is $\gamma = -1$. Triangles correspond to set (c), for which $\sigma_L^2 = 0.25$ and $\gamma = -1.5$. We can see that the predictions (from the SC model) are in good overall agreement with the simulations. It is encouraging that the agreement is not noticeably worse for set (a), which has a much higher amplitude of mass fluctuations on the relevant scale.

We can also compare the predictions of the SC model with simulations for different values of the amplitude of mass fluctuations. In Figures 11 and 12 we have done this, by plotting the flux moments for several different simulation output times. We can see that for most of the range, the predictions work well, for both sets of simulations with different linear slopes (γ). At very low amplitudes σ_L^2 , the simulations will still be dominated by the effect of the initial particle grid, so

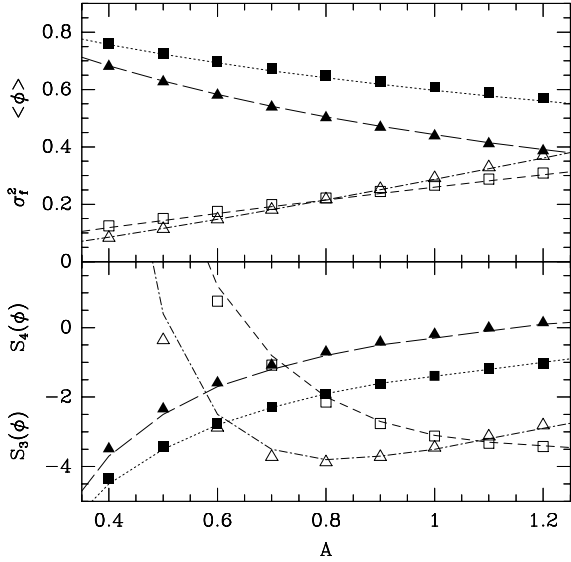


Figure 10. The first 4 moments of the flux in simulation set (a) (squares) and set (d) (triangles) compared to the appropriate analytical predictions (lines), as a function of A . The top panel shows the mean flux $\langle\phi\rangle$ (closed figures) and the variance σ_f^2 (open figures). The bottom panel shows the hierarchical skewness $S_3(\phi)$ (closed figures) and the kurtosis $S_4(\phi)$ (open figures). All results are in real-space.

that the differences we see for the lowest amplitude output are not surprising. For high values of σ_L^2 , the SC predictions start to break down, with S_3 and S_4 being most affected. This shows that we must be careful when interpreting results which appear to indicate high values of σ_L^2 .

Ultimately, the real test of how far we should trust our analytic methods should come from comparisons with hydrodynamic simulations, and in particular those that been run at resolutions high enough to resolve the Jean's scale. In such simulations (e.g., Bryan et al 1998, Theuns et al 1998) it is found that quantities such as the mean effective optical depth are indeed sensitive to resolution. In the SC model computations, although the smoothing scale does not enter directly as a parameter, the quantities which do enter, γ and σ_L^2 are dependent on it. A smaller Jean's scale will yield higher values of σ_L^2 , and as we can see from the N-body only tests of Figs. 11 and 12, the accuracy of our approximations can vary widely. The first three moments of the flux are recovered within $\sim 10-20\%$, for $\sigma_L^2 \simeq 4$ and below (for which the non-linear variance in the density field, $\sigma^2 \sim 10$). The kurtosis of the flux has a much larger error, although as we will see later some non-Gaussian models have such a different S_4 , that it should still be detectable. A more direct test involves consideration of results from the higher resolution version of the simulations from set (a). This simulation has a higher mass resolution by a factor of ~ 12 . When we use the same filter size as for set (a), we find that the flux moments do not change. If we decrease the filter size by $12^{\frac{1}{3}}$ to $0.13 h^{-1}\text{Mpc}$, (at which scale $\sigma_L^2 = 3.8$), the SC predictions for the mean flux and variance are still accurate to better than 10%, but the prediction for $S_3(\phi)$ is -2.3 , when the

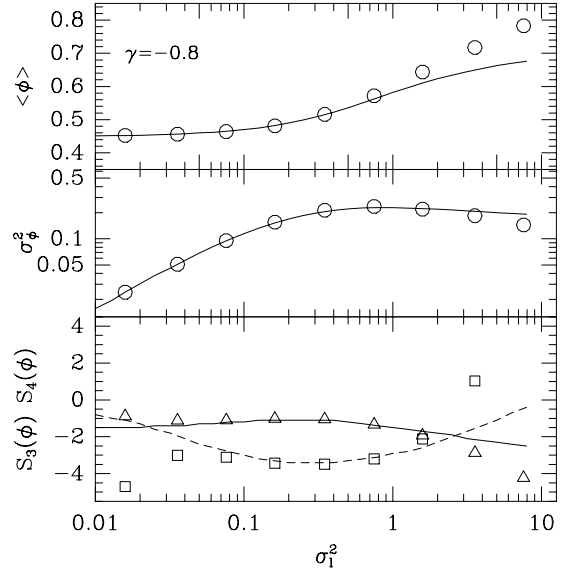


Figure 11. The mean flux (top panel), variance (middle), S_3 (triangles), and S_4 (squares) for simulation set (b), as a function of σ_f^2 . We have used $A = 0.8$ and $\beta = 1.6$ to generate the spectra. The corresponding predictions of the spherical collapse model are shown as lines. All results are in real space.

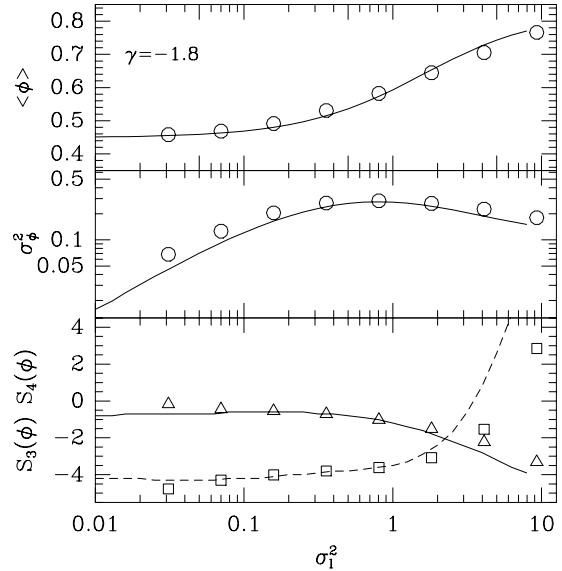


Figure 12. The mean flux (top panel), variance (middle), S_3 (triangles), and S_4 (squares) for simulation set (c), as a function of σ_f^2 . We have used $A = 0.8$ and $\beta = 1.6$ to generate the spectra. The corresponding predictions of the spherical collapse model are shown as lines. All results are in real space.

simulation value is -3.0 , and the SC $S_4(\phi)$ is -1.0 when the simulation gives $+2.4$.

One way of looking at these statistics is as constraints on the unknown parameters which describe the density field, γ and σ_L^2 . If we return to Fig. 10 we note that the results for σ_f^2 are quite similar for both sets of simulations. This can be also seen in Fig. 2, if we look at the results for different values

β and A . The mean flux or the skewness seem to respond more sensitively to σ_L . We can also see this by examining Figures 1 and 3, where for small σ_L the skewness of the flux is a much better indicator of γ than the mean flux. This then changes at $\sigma_L^2 \simeq 2$ where there is a degeneracy in $S_3(\phi)$ for different values of γ , while $\langle\phi\rangle$ seems to give different predictions. It is interesting that, although one model has a larger amplitude of mass fluctuations, the variance in the flux is not systematically higher or lower in one model than the other, but instead which is higher depends on A . We also note that the kurtosis becomes quite large for small values of A . Although the accuracy of our predictions for S_4 decreases as σ_L^2 becomes large (see above), when σ_L^2 is moderate, the rapid increase in S_4 seen for small values of A is reproduced, even for values as large as $S_4 \simeq 100$.

5.5 Comparisons with the mean flux held fixed

We have seen in Fig. 6 that if we choose a specific value of A , the flux statistics can change fairly drastically if we add or remove the effects of peculiar velocities or thermal broadening. When working with observational data, the value of A is at best only known from estimates of the individual parameters in equation (3), Ω_b , Γ , $H(z)$ to within a factor of 2. It would therefore be a good idea if we could fix A directly using Ly α observations. In principle, when working within the formalism we have adopted in this paper, there are 4 unknown quantities, γ , σ_l , A and β . It has already been found in Croft et al. (1998a) that a convenient way of effectively determining the correct value of A to use in numerical simulations is to choose the value which yields the observed mean flux $\langle\phi\rangle$. We carry out the same procedure here, so that when evaluating our predictions we make sure that $\langle\phi\rangle$ is a fixed value. In Fig. 13 we show results for three different values of $\langle\phi\rangle$, 0.6, 0.7, and 0.8, which are in the range measured from observations at $z = 2 - 4$. In the top panel, we show the value of A required for each value of $\langle\phi\rangle$, as a function of σ_l^2 . All results are in redshift-space, except for $\langle\phi\rangle = 0.7$, which we also show in real-space. We can see that once the mean flux is held fixed, the one-point moments of the flux change only little with the addition of redshift distortions. In particular we find that the normalized hierarchical moments, $S_3(\phi)$ and $S_4(\phi)$ are practically identical in real and redshift-space.

In Fig. 14 we concentrate on $\langle\phi\rangle = 0.7$ and show the variation with γ , again in redshift-space. We can see that when the fluctuations in the underlying density field are large, the variance and skewness tend to asymptotic values. As expected, more negative values of γ , will produce spikier, more saturated absorption features and so give a larger variance and skewness. To see the maximum values that this tendency will produce, we can consider the fact that ϕ can only lie between 0 and 1. There is therefore a limit to the level of clustering, given a specific value of the $\langle\phi\rangle$. This will occur if a spectrum contains only pixels which have either $\phi = 1$ or $\phi = 0$ (either no absorption or saturated). If the a fraction f of the spectrum has $\phi = 1$, and the rest, a fraction $(1 - f)$, has $\phi = 0$, then $\langle\phi\rangle = f$. Using the definition of σ_ϕ^2 and $S_3(\phi)$ in equations (26) and (27), we find that the variance in this case is

$$\sigma_\phi^2 = \frac{1}{f} - 1 = \frac{1}{\langle\phi\rangle} - 1, \quad (37)$$

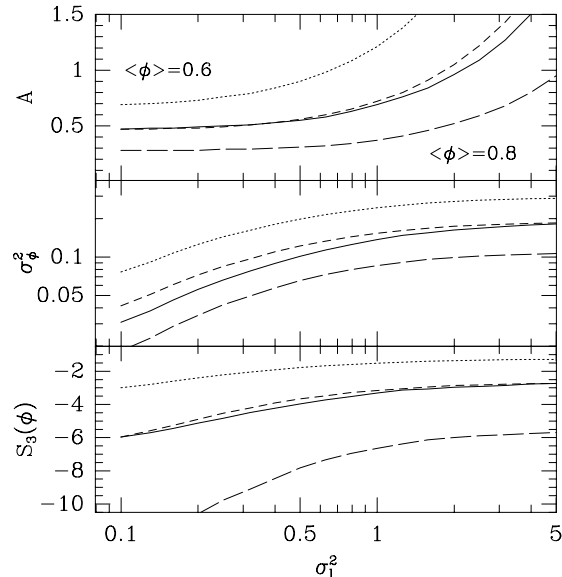


Figure 13. Variation of the SC predictions (variance, middle panel and skewness, bottom panel) with σ_L^2 for a fixed mean flux. In the top panel we show the value of A needed to give mean flux $\langle\phi\rangle = 0.6$ (dotted line), 0.7 (short-dashed line), and 0.8 (long-dashed line). All results are in redshift-space (with thermal broadening) except for the continuous line which represents results for $\langle\phi\rangle = 0.7$ in real-space.

and the normalized hierarchical skewness is given by

$$S_3(\phi) = \langle\phi\rangle \left(\frac{1}{\langle\phi\rangle} - 1 \right) + \frac{(\langle\phi\rangle - 1)}{([1/\langle\phi\rangle] - 1)^2}. \quad (38)$$

For $\langle\phi\rangle = 0.7$, as in Fig. 14, the maximum possible $\sigma^2\phi = 0.43$ and $S_3(\phi) = -1.33$.

6 DISCUSSION

The methods we have introduced in this paper are primarily meant to be used as tools in the study of structure formation. The predictive techniques for the one-point statistics should be most useful when combined with information on clustering as a function of scale (two-point statistics), which we explore in a separate paper. As far as applying our formalism to observations is concerned, the one-point statistics we have discussed should in principle require data which resolves the structure in the forest, at least at the level of the Jean's scale, or the thermal broadening width. This would include Keck HIRES data (e.g., Kirkman & Tytler 1997) or other data with a spectral resolution better than $\sim 10-15 \text{ km s}^{-1}$. Use of lower resolution data effectively involves smoothing along the line-of-sight, and we leave the treatment of this anisotropic smoothing window to future work.

At the simplest level, one could use our predictions for the one-point moments to compare directly to observations. For example, given a measurement of the mean flux (say $\langle\phi\rangle = 0.7$), and a value for slope γ , one can use Fig. 14 to infer the predictions of gravitational instability for $S_3(\phi)$ and $S_4(\phi)$, and then check them against the observed values.

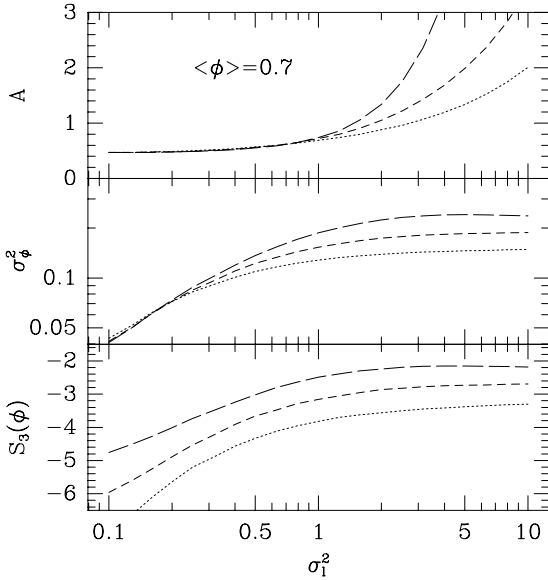


Figure 14. Variation of the SC prediction for the flux moments, with a fixed mean flux, as in Fig. 13, except this time for three different values of the linear slope γ . The dotted, short-dashed and long-dashed lines show the predictions for $\gamma = 0, -1$ and -2 respectively. All results in redshift-space, and $\langle\phi\rangle = 0.7$ for all curves.

This sort of test, while being suitable for checking whether predictions are generally compatible with Gaussian initial conditions, and gravitational instability, is unlikely to be useful for discriminating between popular Gaussian models, which have similar one point flux PDFs. For example, there is little difference in the behaviour of the flux moments for two models with different values of γ shown in Figs. 11 and 12 (see also the small differences between $\Omega = 1$ CDM and $\Omega = 0.4$ CDM in Rauch et al. 1997). We therefore advertise our one-point analytic predictions as being more suitable for making wide searches of parameter space in order to ascertain the broad statistical trends expected in gravitational instability models (for example, see below for the evolution of the moments with redshift). Direct comparisons with observational data will be more fruitful when carried out with two point statistics. We will explore these, and how the analytic methods we have developed here can be applied to them, in a future paper. For the moment, several obvious applications of our techniques for making one-point predictions suggest themselves, and we discuss these now. We also discuss the accuracy of the density evolution predictions, and compare the present work to that of others.

6.1 Non-Gaussian initial conditions

There is a large parameter space of non-Gaussian PDFs to choose from (see Fosalba, Gaztañaga & Elizalde 1998). Here we will take a conservative approach and choose a model with *mild* non-Gaussianities, with hierarchical correlations, i.e., constant S_J , so that the cumulants $k_J \simeq k_2^{J-1}$. They tend to the Gaussian result as $k_2 \rightarrow 0$ more quickly than the dimensional scaling $k_J \simeq k_2^{J/2}$. As an illustrative example, we will show results for a PDF based on the well

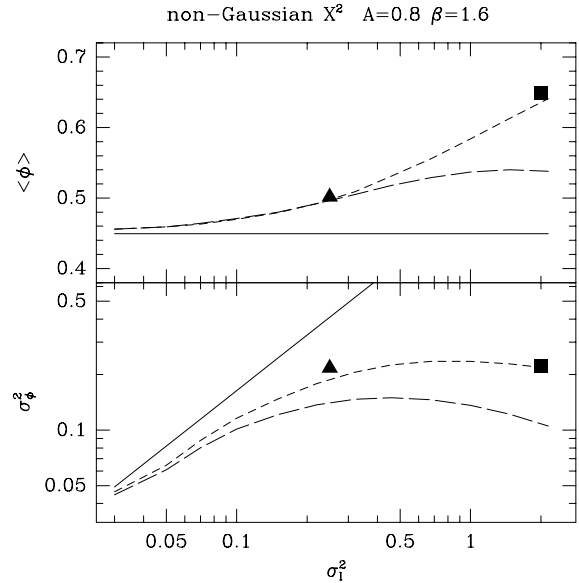


Figure 15. A comparison of Gaussian and non-Gaussian models. Mean flux $\langle\phi\rangle$ and variance σ_ϕ^2 (bottom) are plotted as a function of the linear variance σ_L^2 for $\gamma = 1$, $A = 0.8$ and $\beta = 1.6$. The short-dashed and long-dashed lines show the SC predictions for a Gaussian model and a non-Gaussian PT3 model respectively. Symbols correspond to the Gaussian simulations, with the squares representing set (a) (which has $\gamma \simeq 1$) and the triangles set (d) (which has $\gamma \simeq -1.5$). The continuous lines are the perturbative predictions of Section 4.3. All results are in real-space.

known chi-squared distribution (see e.g., Fosalba, Gaztañaga & Elizalde 1998 for details), also known as Pearson's Type III (PT3) PDF or Gamma PDF:

$$P(\rho) = \frac{\rho^{1/\sigma^2-1}}{\Gamma(1/\sigma^2)(\sigma^2)^{1/\sigma^2}} \exp\left(-\frac{\rho}{\sigma^2}\right), \quad (39)$$

for $\rho \equiv 1 + \delta \geq 0$. This PDF has $S_3 = 2$ and $S_4 = 6$ (in general $S_J = [J - 1]!$). The number of the chi-square degrees of freedom, N , in the discrete version of this distribution would correspond to $N = 2/\sigma^2$. It is not difficult to build a non-Gaussian distribution with arbitrary values of S_3 or S_4 , but to keep the discussion simple we will just concentrate on the PT3 model. This model is not only mildly non-Gaussian, in the sense of being hierarchical, but also has moderate values of S_J (e.g., for comparison gravity produces $S_3 = 34/7$ from Gaussian initial conditions and unsmoothed fluctuations).

A possible motivation for introduction of the PT3 could be the isocurvature CDM cosmogony presented recently by Peebles (1998), which has as initial conditions a one-point unsmoothed PDF given by a chi-square distribution with $N = 1$ (i.e. a PT3 with $\sigma^2 = 2$). Smoothing would introduce higher levels of non-Gaussianities through the two-point function, so this is a conservative approach. A more generic motivation follows from the arguments presented in Fosalba, Gaztanaga & Elizalde (1998), who find that this distribution plays a central role in non-Gaussian distributions that arise from combinations of a Gaussian variables.

In Figures 15-16 we compare the Gaussian and non-Gaussian PT3 predictions. As can be seen, even in this mildly non-Gaussian model the predictions are quite dif-

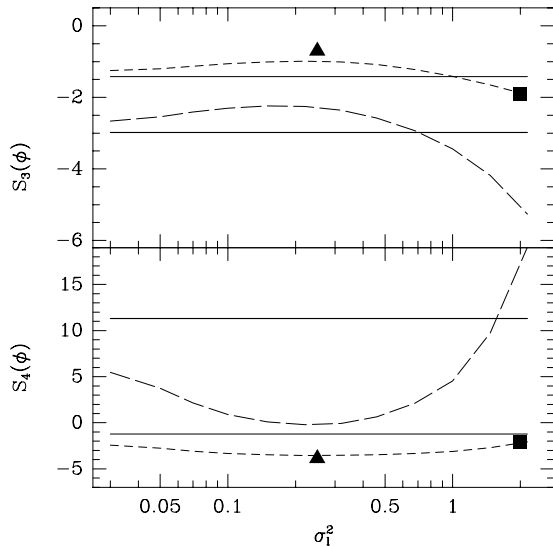


Figure 16. A comparison of Gaussian and non-Gaussian models. We plot the skewness S_3 and kurtosis S_4 . The symbols and line types are the same as in Fig. 15. The continuous lines are the perturbative predictions, which are different for the Gaussian (thin line) and non-Gaussian (thick line) models.

ferent and can be clearly distinguished from the Gaussian simulations (symbols). The SC predictions for Gaussian initial conditions have been evaluated for $\gamma = -1$. The squares correspond to simulation set (a), which also have $\gamma \simeq -1$. The triangles are from set (c) and have $\gamma = -1.5$. This value of γ is different from that used for the SC Gaussian predictions, although the simulation point for σ_ϕ^2 is still closer to them than the non-Gaussian predictions.

The leading order perturbative predictions, shown as continuous lines in the Figures, are the same for $\langle\phi\rangle$ and σ_ϕ^2 , because the non-Gaussian model is hierarchical. However for S_3 and S_4 the predictions are different. It is easy to show that to leading order the (hierarchical) non-Gaussian model predictions are given by equation (32) with:

$$\begin{aligned} S_3 &= S_3(IC) + S_3(G) \\ S_4 &= S_4(IC) + S_4(G) + 4S_3(G)S_3(IC) \end{aligned} \quad (40)$$

where $S_3(IC)$ and $S_4(IC)$ are the initial conditions [$S_J(IC) = (J-1)!$ for PT3] and $S_3(G)$ and $S_4(G)$ are the leading order gravitational values: $S_3(G) = 34/7 + \gamma$ and $S_4(G) = 60712/1323 + 62/3\gamma + 7/3\gamma^2$. As can be seen in Fig. 16 the perturbative values are only reached asymptotically as $\sigma_L \rightarrow 0$. The skewness S_3 is significantly lower in the PT3 model and the kurtosis S_4 is much larger, changing from $S_4 \simeq -2$ in the Gaussian model to $S_4 \simeq 20$ in the non-Gaussian one.

Fig. 17, shows a comparison between the Gaussian and PT3 models, for a fixed mean flux. We noted previously (e.g., Fig 13) the useful fact that there is little difference between the predictions with or without redshift distortions when the mean flux is fixed in this way. Fortunately, this is not the case for non-Gaussianities, as we can see here. The results change considerably if we assume different initial conditions.

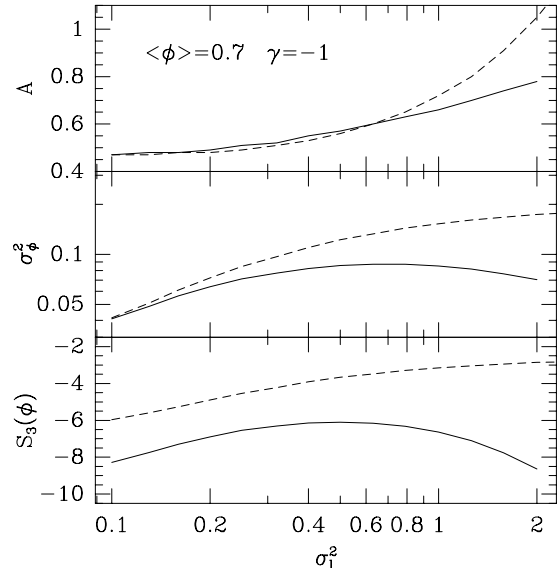


Figure 17. Comparison between non-Gaussian and Gaussian predictions when $\langle\phi\rangle$ is held fixed. We plot the optical depth amplitude A (top), variance σ_ϕ^2 and skewness $S_3(\phi)$ (bottom) as a function of the linear variance σ_L^2 for a mean flux $\langle\phi\rangle = 0.7$, $\gamma = 1$, and $\beta = 1.6$. The short-dashed and continuous lines show the predictions of the Gaussian and non-Gaussian PT3 models. These results are in redshift-space.

6.2 Redshift evolution

We can see from equation (3) that A will change strongly with redshift, and that there will be a dependence on cosmology through the variation in $H(z)$. We can investigate how the one-point flux statistics will vary using our formalism. We compute the evolution of $H(z)$ and σ_L^2 and show the results for $\Omega_0 = 1$ and three different values of γ in Fig. 18. We can see that both σ_ϕ^2 and $S_3(\phi)$ become much smaller as the mean absorption falls. In these figures we are assuming that γ is not changing as a function of redshift, or equivalently that the smoothing scale is fixed in comoving h^{-1} Mpc.

In Fig. 19 we plot the results for three different background cosmologies, two flat models, one with $\Omega = 1$ and one with $\Omega_0 = 0.3$ and $\Omega_\Lambda = 0.7$, as well as an open model with $\Omega_0 = 0.3$. All models have the same γ , σ_L and the same mean flux ($\langle\phi\rangle = 0.66$) at $z=3$. We can see that there is virtually no visible dependence on cosmology in the plot. The main source of variation in A which we have not included, is the evolution of the photoionization rate Γ , which will change as the population of sources for the ionizing background changes. From Fig. 19 it is evident that inferences about the evolution of the UV background should be fairly insensitive to the assumed cosmology. We can see why this is so by looking at Fig. 20, where we plot the evolution of A and σ_L^2 separately. If both quantities are fixed in the middle of the z range as we have done, then the changes over the range of validity of the FGPA ($z \gtrsim 2$) are small.

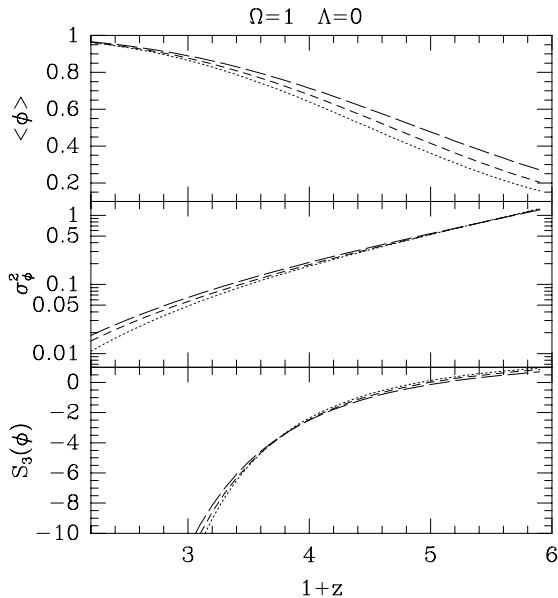


Figure 18. The variation of the one-point statistics with redshift, for three different values of γ , 0 (dotted line), -1 (short-dashed line), and -2 (long-dashed line). The parameter $A = 1.2$ at $z = 3$ in all cases, and $\sigma_L^2 = 2$. Results are for $\Omega = 1$ and are in redshift-space with thermal broadening.

6.3 The bias between flux and mass fluctuations

In analogy with galaxy bias, we can define the bias of the flux with respect to mass fluctuations as

$$b = \sqrt{\frac{\sigma_\phi^2}{\sigma_\rho^2}}. \quad (41)$$

Unlike the case with galaxy bias, we can easily predict this quantity analytically using our formalism. We can choose between two sorts of bias, either the bias between the linear ρ , or the nonlinear ρ . In Fig. 21 we have plotted both of these as a function of the variance in the flux, σ_ϕ . As we are dealing with one-point statistics in this paper, we do not discuss the scale dependence of bias. However we will do so in Paper II in this series (Gaztañaga & Croft 1999). We should point out though that in Croft et al. (1998a), it was found that the shape of a two-point clustering statistic of the flux (in that case the power spectrum) follows well that of the linear mass. The bias between the two was found in that paper by using a procedure which involved running numerical simulations set up with the power spectrum shape measured from observations and comparing the clustering level in simulated spectra with the observed clustering. In this paper, we can find the bias level in a simpler fashion. We note that for small values of the fluctuation amplitude, b tends towards the values predicted by perturbation theory (Section 4.3). For larger values, such as those likely to be encountered in observations, a fully non-linear treatment, such as the one presented here, is needed.

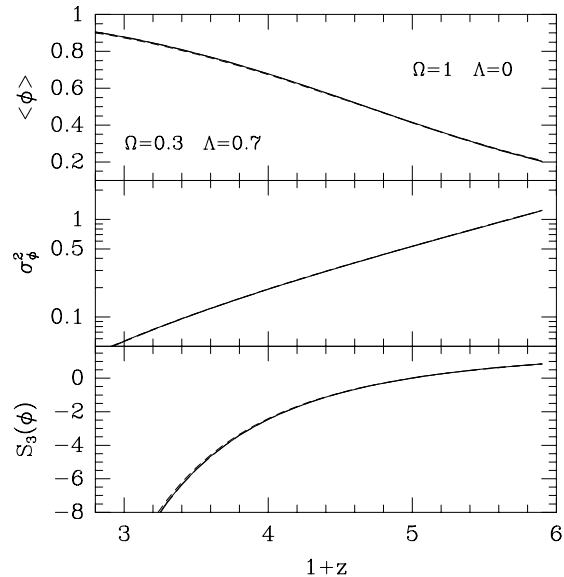


Figure 19. The variation of the one-point statistics with redshift, for three different cosmologies. We have plotted results for $\Omega = 1$ (solid line), $\Omega_0 = 0.3, \Omega_\Lambda = 0$ (short-dashed line), and $\Omega_0 = 0.3, \Omega_\Lambda = 0.7$ (long-dashed line). In all cases, $\sigma_L^2 = 2$ and $\langle \phi \rangle = 0.66$ at $z = 3$. Results are in redshift-space with thermal broadening.

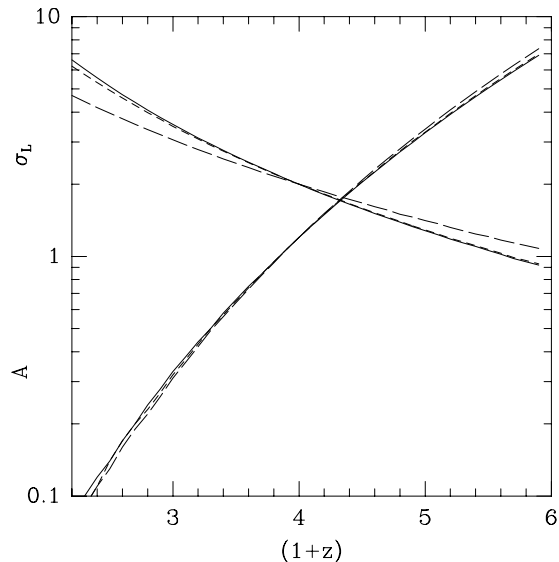


Figure 20. Variation with redshift of A and σ_L^2 . Results have been plotted for 3 different cosmologies, $\Omega = 1$ (solid line), $\Omega_0 = 0.3, \Omega_\Lambda = 0$ (short-dashed line), and $\Omega_0 = 0.3, \Omega_\Lambda = 0.7$ (long-dashed line).

6.4 Accuracy of the approximations for density evolution

We have seen (e.g., Fig. 7) that the predictions for the PDF have the right qualitative features (as a function of γ and σ_L) but do not reproduce it in all its details, even around $\delta = 0$, because the SC is just a local approximation and

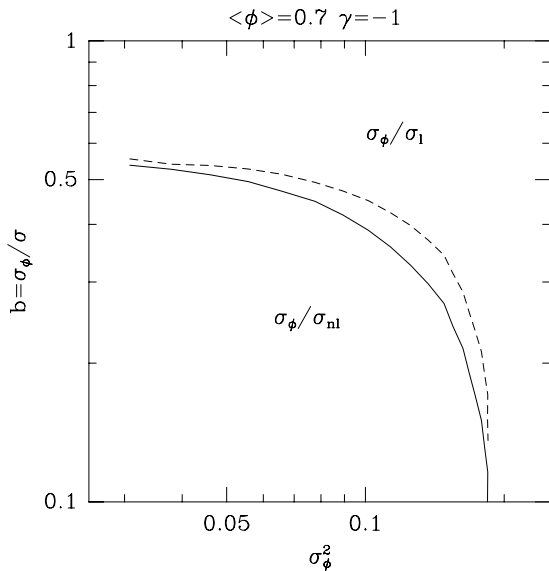


Figure 21. The bias between flux and mass fluctuations. We show the bias (see equation [41]) between the flux and the linear mass (σ_l) as a dotted line and the bias between the flux and the non-linear mass (σ_{nl}) as a solid line. Both these quantities are plotted as a function of the observable σ_ϕ^2 . The statistics of ϕ have been computed in redshift space with thermal broadening, for $\langle\phi\rangle = 0.7$, $\sigma_L^2 = 2$ and $\gamma = -1$.

does not include shear. The results of FG98 indicate that the statistics of the weakly non-linear density moments are dominated by the local dynamical contribution to the evolution of the PDF, and shear forces are subdominant (they tend to cancel out when taking the mean). We find here that a similar cancellation occurs when considering the PDF of the flux, ϕ , even when $\sigma_L \gtrsim 1$.

Regarding the predictions for the 1-point moments of the flux, we have checked that the Spherical Collapse (SC) model yields almost identical results to the Generalized Zel'dovich Approximation (GZA), in Eq[A10], with $\alpha = 21/13$. This is true both in real and redshift-space, and also holds for the prediction of the velocity divergence θ . This is an interesting result because although the SC model is better motivated from the theoretical point of view, the GZA model is much simpler to implement. In particular the GZA model provides us with analytical expressions for the PDF (i.e., equation [A26] and Fig. 8), which can be used in practice to make the predictions.

As shown in Fosalba & Gaztañaga (1998b) the SC approach to modelling non-linearities does not work as well for θ as for ρ . In particular, it was found that the next to leading order (or loop) non-linear corrections are not as accurate, indicating that tidal effects are more important for θ . This could partially explain why the redshift distortion modelling (see Fig. 6) requires the addition of an extra velocity dispersion in order to match the results of simulations.

6.5 Comparison to other work

The first attempts to constrain cosmology using the Ly α forest focussed on comparisons between simulated data gen-

erated with specific cosmological models and observational data, using traditional line statistics. When the simulated and observed spectra are decomposed into a superposition of Voigt-profile lines, the distribution of column densities of these lines and the distribution of their widths (“b-parameters”) can be reasonably well reproduced by gravitational instability models (e.g., Davé et al. 1997, although see Bryan et al. 1998). In the context of these models, the line parameters do not have a direct physical meaning, as these statistics were intended to describe discrete thermally broadened lines. It is possible to use these traditional statistics to characterise the amount of small scale power in the underlying density field, for example (see e.g., Hui, Gnedin & Zhang, Gnedin 1998). However, statistics which are more attuned to the continuous nature of the flux distribution and the underlying density field have advantages, as well as promising to be more sensitive discriminants, continuous flux statistics can be designed to be less affected by noise and choice of technique than profile fitting.

As the modern view of the Ly α is essentially an outgrowth of structure formation theory, it makes sense to borrow statistical analysis techniques used in the study of the galaxy distribution. Unlike the galaxy distribution, however, the Ly α forest offers a truly continuous distribution of flux, with no shot noise (albeit in 1 dimension), and a well motivated theoretical relationship between the observed flux and the underlying mass.

So far, analysis of spectra using such continuous flux statistics has mainly involved specific cosmological models, and direct comparison of simulations with observations. The mean flux, $\langle\phi\rangle$ is the most obvious flux statistic to calculate. Its measurement from observations has been carried out by several authors (e.g. Press, Rybicki & Scheider, 1993, Zuo & Lu 1993), and there is an extensive discussion in the literature about what is usually quoted as the mean flux decrement, $D_A = 1 - \langle\phi\rangle$, or the mean effective optical depth, $\bar{\tau}_{\text{eff}} = -\ln\langle\phi\rangle$

The probability distribution of the flux has been investigated by Miralda-Escudé et al. (1996), Croft et al. (1996), Cen (1997), Rauch et al. (1997), Zhang et al. (1998), and Weinberg et al. (1998). Other statistics such as the two point correlation function of the flux have been introduced (Zuo & Bond 1994), the power spectrum of the flux (Croft et al. 1998a, Hui 1999, the two point pdf of the flux (Miralda-Escudé et al. 1997), and the number of times a spectrum crosses a threshold per unit length (Miralda-Escudé et al. 1996, Croft et al. 1996, Weinberg et al. 1998). Methods have been developed to reconstruct properties of the underlying mass distribution, such as the matter power spectrum (Croft et al. 1998a, Hui 1999, using our theoretical assumptions for the relation between mass and flux. A technique for carrying out a direct inversion from the flux to the mass distribution has been described by Nusser and Haehnelt (1998). In the present paper, we emphasise the use of statistics which have been used extensively in the study of galaxy clustering, in particular the higher order moments (e.g., Gaztañaga & Frieman 1994). These statistics, and their behaviour when used to quantify the evolution of density perturbations in the quasil-linear regime have been the subject of much attention. It would seem that extending their use to the study of the Ly α forest may offer us a good chance to combine our

knowledge of gravitational instability with that of the IGM and in doing so make progress in both disciplines.

On the predictions side, many pieces of analytic work have been carried out which incorporate the dominant physical processes involved in producing high-redshift Ly α absorption (processes summarized in Section 2). The studies' most important differences have been in the schemes used to follow the evolution of density perturbations. These have included linear theory (Bi 1993, Bi, Ge & Fang 1995) the lognormal approximation (Gnedin & Hui 1996, Bi & Davidson 1997), and the Zel'dovich Approximation (McGill 1990, Reisenegger & Miralda-Escudé 1995, Hui, Gnedin & Zhang 1997). Unlike these approximations, the SC model used in this paper is able to reproduce exactly the perturbation theory results for clustering. This accuracy makes it useful for calculating high-order statistics of the flux, in our search for the signatures of gravitational instability. It is important to realize that we have not used the SC model to make simulated QSO Ly α spectra, but that we have used its predictions for the properties of the mass to predict the statistics of the Ly α flux. With such an approach (similar to that taken by Reisenegger & Miralda-Escudé 1995) we can quickly and easily vary parameters in order to explore for example the dependence of a particular statistic on redshift (Section 6.2). Some tasks which previously required numerical simulations, such as finding the bias between density and flux fluctuations (e.g., Croft et al. 1998ab), can be carried out analytically.

The fully non-linear analysis we have described in this paper will allow one to carry out many analyses of clustering where the precise relationship between the statistics of the mass and the flux is important. This includes attempts to constrain the cosmic geometry from the clustering measured between adjacent QSO lines of sight (e.g., McDonald & Miralda-Escudé 1999 Hui, Stebbins & Burles 1999. In such situations, a non-linear theory of redshift distortions in the Ly α forest and of the bias between the fluctuations in the observed flux and the mass, such as we have presented in this paper should be very useful.

7 SUMMARY AND CONCLUSIONS

We have presented a fully non-linear analytical treatment of the one-point clustering properties of the high- z Ly α forest in the gravitational instability scenario. The formalism we have presented should prove to be a useful tool for studying the forest, and has immediate application to the calculation of two-point statistics (see Paper II). The two main ingredients we have used are the Spherical Collapse model (SC) or shear-free approximation for the evolution of density perturbations, and the Fluctuating Gunn-Peterson Approximation for the relation between density and Ly α optical depth. The predictions for the one-point clustering of the mass made using the SC model depend only on two parameters, σ_L^2 and γ . These are, respectively, the linear variance of density fluctuations, and the local slope of the linear correlation function. In the FGPA, the relation between the mass distribution and Ly α forest optical depth is largely governed by one parameter, A , which can be set by appealing to observational measurements of the mean flux. The predictions of the SC model for the density are typically quite non-linear ($\sigma^2 \sim 2$

or more). While these predictions are not expected to be accurate for the high density tail of the distribution, the weighting of the FGPA relation means that the statistics of the flux are governed by the (quasi-linear) density regime where the SC is accurate. The Ly α forest is therefore well suited to study using such an approximate analytical technique.

We note that the analytical predictions can be used in tests of the picture of Ly α forest formation and the applicability of the FGPA. With the extra information afforded by the two-point statistics and considering the evolution of clustering as a function of redshift, it will be possible to look for the signatures of any deviation from the theoretical picture. Consistency tests for the gravitational instability scenario include checking the evolution of the moments as a function of redshift, the scaling of the hierarchical moments, and their dependence on scale.

We plan to use our predictive techniques in future work to extract information from observations, using both one-point and two-point statistics. In the present paper, we have concentrated on developing an analytical framework for studying the clustering of the transmitted flux in the forest region of QSO spectra. Some of the results of our present exploration of one-point statistics include the following:

- Using our formalism we are able to estimate the bias between mass and flux fluctuations without resorting to simulations.
- We can make predictions for the clustering properties of the Ly α forest flux in both Gaussian and non-Gaussian models. We find large differences between the two in an example case.
- In the limit of small fluctuations, our non-linear analytical treatment converges to the same results as those from Perturbation Theory calculations.
- For larger fluctuations, where Perturbation Theory is no longer valid, we find our treatment to give accurate results compared to statistics evaluated from N-body simulated spectra. These predictions are most accurate when the linear variance of the density field is ~ 4 and below. For values above this, the qualitative behaviour of the high order moments is reproduced.
- We can follow the evolution of the one-point statistics of the flux as a function of redshift. We find that the difference between predictions for different cosmologies is small, so that comparison with observations should be useful in constraining the evolution of the ionizing background intensity.
- If we normalise our predictions so that the mean flux is held fixed (for example to the observed value), we find that the statistics of the flux are relatively insensitive to the effects of redshift distortions induced by peculiar velocities or thermal broadening. This is most valid for the higher order normalised hierarchical moments.

The high- z Ly α forest is amenable to study using analytical treatments, a fact which gives it great value as a probe of structure formation. Application of analytical theory to measurements from the many observational datasets currently available promises to reveal much, both about the validity of our theoretical assumptions, and about cosmology.

Acknowledgments

We thank George Efstathiou for the use of his P³M N-Body code. We also thank Jasjeet Bagla and Pablo Fosalba for useful discussions, and the anonymous referee for suggestions which improved the paper. EG acknowledges support from CSIC, DGICYT (Spain), project PB93-0035, and CIRIT, grant GR94-8001 and 1996BEAI300192. RACC acknowledges support from NASA Astrophysical Theory Grant NAG5-3820 and CESCA for support during a visit to the IEEC.

8 REFERENCES

- Baugh, C.M., Gaztañaga, E., & Efstathiou, G., 1995, MNRAS, 274, 1049
- Bi, H.G., Boerner, G., Chu, Y., 1992, A & A, 266, 1
- Bi, H.G. 1993, ApJ, 405, 479
- Bi, H., Ge, J., & Fang, L.-Z. 1995, ApJ, 452, 90
- Bi, H.G. & Davidsen, A. 1997, ApJ, 479, 523
- Bechtold, J., Crotts, A. P. S., Duncan, R. C., & Fang, Y. 1994, ApJ, 437, L83
- Bernardeau, F., 1992, ApJ, 392, 1
- Bernardeau, F., 1994, A&A, 291, 697
- Bernardeau, F., & Kofman, L., 1995, ApJ, 443, 479
- Bryan, G.L., Machacek, M., Anninos, P., Norman, M.L., 1998, ApJ, 517, 13
- Cen, R., 1997, 479, L85
- Cen, R., Miralda-Escudé, J., Ostriker, J.P., & Rauch, M. 1994, ApJ, 437, L9
- Croft, R.A.C., & Efstathiou, G., 1994, MNRAS, 267, 390
- Croft, R.A.C., Weinberg, D.H., Hernquist, L. & Katz, N. 1996, In : "Proceedings of the 18th Texas Symposium on Relativistic Astrophysics and Cosmology", eds. Olinto, A., Frieman, J., & Schramm, D.N.
- Croft, R.A.C., Weinberg, D.H., Katz, N., & Hernquist, L. 1997, ApJ, 488, 532
- Croft, R.A.C., Weinberg, D.H., Katz, N., & Hernquist, L. 1998a, ApJ, 495, 44
- Croft, R.A.C., Weinberg, D.H., Pettini, M., Hernquist, L., & Katz, N. 1999, ApJ 520, 1
- Crotts, A.P.S., & Fang, Y., 1998, ApJ, 497, 67
- Davé, R., Hernquist, L., Weinberg, D. H., & Katz, N. 1997, ApJ, 477, 21
- Davé, R., Hernquist, L., Katz, N., & Weinberg, D. H., 1999, ApJ, 511, 521
- Dinshaw, N., Impey, C. D., Foltz, C. B., Weymann, R. J., & Chaffee, F. H. 1994, ApJ, 437, L87
- Dinshaw, N., Foltz, C. B., Impey, C. D., Weymann, R. J., & Morris, S. L. 1995, Nature, 373, 223
- Efstathiou, G., & Eastwood, J.W., 1981, MNRAS, 194, 503
- Efstathiou, G., Bond, J.R., & White, S.D.M., 1992, MNRAS, 258, 1p
- Efstathiou, G., Davis, M., White, S.D.M., & Frenk, C.S., 1985, ApJS, 57, 241
- Fardal, M., & Shull, M., 1993, ApJ, 415, 524
- Fosalba, P., & Gaztañaga, E., 1998a, MNRAS, 301, 503 (FG98)
- Fosalba, P., & Gaztañaga, E., 1998b, MNRAS, 301, 535
- Fry, J.N., & Gaztañaga, E., 1993, ApJ, 413, 447
- Gaztañaga, E., & Baugh, C.M., 1995, MNRAS, 273, L5
- Gaztañaga, E., & Croft, R.A.C., 1999, *in preparation* (Paper II)
- Gaztañaga, E., & Fosalba, P., 1998, MNRAS, 301, 524 astro-ph/9712095
- Gaztañaga, E., & Frieman, J.A., 1994, MNRAS, 425, 392
- Gnedin, N. Y. & Hui, L. 1996, ApJ, 472, L73
- Gnedin, N. Y., & Hui, L. 1998, MNRAS, 296, 44
- Gunn, J.E., & Peterson, B.A. 1965, ApJ, 142, 1633
- Haiman, Z., Thoul, A., & Loeb, A., 1996, ApJ, 464, 523
- Hernquist L., Katz N., Weinberg D.H., & Miralda-Escudé J. 1996, ApJ, 457, L5
- Hockney, R.W., & Eastwood, J.W., 1988, Computer Simulation Using Particles, Bristol: Hilger
- Hu, E.M., Kim, T-S., Cowie, L.L., Songaila, A., & Rauch, M., 1995, AJ, 110, 1526
- Hui, L., 1999, ApJ, 516, 519
- Hui, L., & Gnedin, N. 1997, MNRAS, 292, 27
- Hui, L., Gnedin, N., & Zhang, Y. 1997, ApJ, 486, 599
- Hui, L., Stebbins, A., & Burles, S., 1999, ApJ, 611, L5
- Juszkiewicz, R., Weinberg, D.H., Amsterdamski, P., Chodorowski, M., & Bouchet, F., 1995, ApJ, 442, 39
- Kaiser, N., 1987, MNRAS, 227, 1
- Katz, N., Weinberg D.H., & Hernquist, L. 1996, ApJS, 105, 19
- Kim, T-S, Hu, E.M., Cowie, L.L., Songaila, A., 1997, AJ, 114, 1
- Kirkman, D., & Tytler, D., ApJ, 484, 672
- Kofman, L., Bertschinger, E., Gelb, J.M., Nusser, A., & Dekel, A., 1994, ApJ, 420, 44
- Lu, L., Sargent, W.L.W., Womble, D., & Takada-Hidai, M., 1996, ApJ, 472, 509
- Lynds, C. R., 1971, ApJ, 164, L73
- McDonald, P. & Miralda-Escudé, J. 1998, ApJ, 518, 24
- McGill, C. 1990, MNRAS, 242, 544
- Miralda-Escudé J., Cen R., Ostriker J.P., & Rauch M. 1996, ApJ, 471, 582
- Miralda-Escudé J., Rauch, M., Sargent, W., Barlow, T.A., Weinberg, D.H., Hernquist, L., Katz, N., Cen, R., & Ostriker, J.P., 1997, in: "Proceedings of 13th IAP Colloquium: Structure and Evolution of the IGM from QSO Absorption Line Systems", eds. Petitjean, P., & Charlot, S.,
- Miralda-Escudé J., & Rees, M. J. 1994, MNRAS, 266, 343
- Munshi, D., Sahni, V., & Starobinsky, A.A., 1994, ApJ, 436, 517
- Nusser, A., & Haehnelt, M., 1999, MNRAS, 300, 1027
- Peebles, P.J.E., 1980, The Large-Scale Structure of the Universe. Princeton Univ. Press, Princeton
- Peebles, P.J.E., 1993, Principles of Physical Cosmology, Princeton Univ. Press, Princeton
- Peebles, P.J.E., 1999, ApJ, 510, 531
- Press W.H., Rybicki G.B., Schneider D.P., 1993, ApJ, 414, 64
- Protogeros, Z.A.M., & Scherrer, R.J. 1997, MNRAS, 284, 425
- Rauch, M., Miralda-Escudé, J., Sargent, W. L. W., Barlow, T. A., Weinberg, D. H., Hernquist, L., Katz, N., Cen, R., & Ostriker, J. P. 1997, ApJ, 489, 7
- Rauch, M., 1998, ARAA, in press
- Reisenegger, A. & Miralda-Escudé, J. 1995, ApJ, 449, 476
- Sargent, W.L.W., Young, P.J., Boksenberg, A., Tytler, D. 1980, ApJS, 42, 41

- Scherrer, R., & Gaztañaga, E., 1998, in preparation
- Theuns, T., Leonard, A., Efstathiou, G., Pearce, F.R., Thomas, P.A., 1998, MNRAS, 301, 478
- Wadsley, J. W. & Bond, J.R. 1996, in “Computational Astrophysics”, Proceedings of the 12th Kingston Conference, eds. Clarke, D., West, M., PASP, astro-ph 9612148
- Weinberg, D.H., Hernquist, L., Katz, N., Croft, R., & Miralda-Escudé, J., 1998a, In : Proc. of the 13th IAP Colloquium, Structure and Evolution of the IGM from QSO Absorption Line Systems, eds. Petitjean, P., & Charlot, S., Nouvelles Frontières, Paris, astro-ph/9709303
- Weinberg et al. , 1998b, In: Proceedings of the MPA/ESO Conference ”Evolution of Large Scale Structure: From Recombination to Garching”, astro-ph/9810142
- Zhang Y., Anninos P., & Norman M.L. 1995, ApJ, 453, L57
- Zhang Y., Meiksin, A., Anninos P., & Norman M.L. 1998, ApJ, 495, 63
- Zuo, L. 1992, MNRAS, 258, 36
- Zuo, L., & Bond, J.R., 1994, ApJ, 423, 73
- Zuo, L., & Lu, L., 1993, ApJ, 418, 601

APPENDIX A: NON-LINEAR MAPPING RELATIONS

A1 Unsmoothed relations

A1.1 The density

For small linear fluctuations, a generic mapping can be expressed in a Taylor series:

$$\rho(x) = \mathcal{G}[\delta_L(x)] = \sum_k \frac{\nu_k}{k!} \delta_L^k(x) \quad (\text{A1})$$

where ν_k are the coefficients that define the transformation in this limit. The above mapping can be used to predict the PDF of the evolved field, or directly predict its cumulants. For example, for the skewness we have:

$$\langle \delta^3 \rangle_c = \langle (\mathcal{G} - \langle \mathcal{G} \rangle)^3 \rangle = 3\nu_2 \sigma_L^4 + \mathcal{O}(\sigma_L^6) \quad (\text{A2})$$

where we have made use of the Gaussianity of δ_L . In general we have:

$$\langle \delta^J \rangle_c = S_J \sigma_L^{2(J-1)} + \mathcal{O}(\sigma_L^{2J}). \quad (\text{A3})$$

For the skewness $S_3 = 3\nu_2$, and in general S_J can be given in terms of ν_k (e.g., see FG98 or the original work by Bernardeau 1992, which is in terms of the generating functionals).

For the SC (see below) we have:

$$\begin{aligned} \nu_2 &= \frac{34}{21} \sim 1.62 \\ \nu_3 &= \frac{682}{189} \sim 3.61 \\ \nu_4 &= \frac{446440}{43659} \sim 10.22 \\ \nu_5 &= \frac{8546480}{243243} \sim 35.13 \end{aligned} \quad (\text{A4})$$

These numbers give the correct leading PT contribution to the J th-order cumulants $\langle \delta^J \rangle_C$ for Gaussian IC, e.g.,

$S_3 = 34/7$ (Peebles 1980, §42). The important point to notice here is that although the local mapping is not the exact solution to the evolution of δ (which is in general non-local), it gives the correct clustering properties in the weakly non-linear regime. This is because of the symmetry involved in taking the ensemble average $\langle \dots \rangle$ (Bernardeau 1992). This is also a good approximation for next to leading terms (FG98) and also for non-Gaussian initial conditions (Gaztañaga & Fosalba 1998).

A1.2 Velocity divergence

The density mapping can be used to predict the velocity divergence, defined here as:

$$\theta = \frac{1}{H} \nabla \cdot v \quad (\text{A5})$$

where v is the peculiar velocity field. We can use the continuity equation:

$$\frac{d\rho}{dt} + H\rho\theta = 0 \quad (\text{A6})$$

to express θ as a Lagrangian mapping of δ_L :

$$\theta = \mathcal{G}_v[\delta_L] = -\frac{1}{H\rho} \frac{d\rho}{dt} = -f_\Omega \frac{\delta_L}{\rho} \frac{d\rho}{d\delta_L}, \quad (\text{A7})$$

where $f_\Omega \equiv d \ln D / d \ln a$, comes from applying the chain rule to the derivative of the linear growth factor: $\delta_L = D(t)\delta_{IC}$.

A1.3 The SC model

For large ρ the spherical collapse mapping $\delta = \mathcal{G}[\delta_L]$ can only be expressed in a parametric form through an auxiliary variable ψ :

$$\begin{aligned} \rho^+ &= \frac{9(\psi - \sin \psi)^2}{2(1 - \cos \psi)^3}, \\ \delta_L^+ &= \frac{3}{5} \left[\frac{3}{4} (\psi - \sin \psi) \right]^{2/3}, \end{aligned} \quad (\text{A8})$$

for $\delta_L > 0$, which we call δ_L^+ , and

$$\begin{aligned} \rho^- &= \frac{9(\sinh \psi - \psi)^2}{2(\cosh \psi - 1)^3}, \\ \delta_L^- &= -\frac{3}{5} \left[\frac{3}{4} (\sinh \psi - \psi) \right]^{2/3}, \end{aligned} \quad (\text{A9})$$

for $\delta_L < 0$, which we call δ_L^- . This parametric form complicates the analytical predictions, but it can be implemented numerically. For $\psi = 2\pi$ the transformation becomes singular and ρ and δ diverge. This is the first collapse which occurs at $\delta_L = 3/5(3\pi/2)^{2/3} \simeq 1.686$, as illustrated in Fig. A1. It then bounces back and recollapses in a periodic fashion.

A1.4 The GZA model

Another model we consider for the local transformation is the *Generalized Zel'dovich Approximation* (GZA):

$$\rho = 1 + \delta = \left| 1 - \frac{\delta_L}{\alpha} \right|^{-\alpha}, \quad (\text{A10})$$

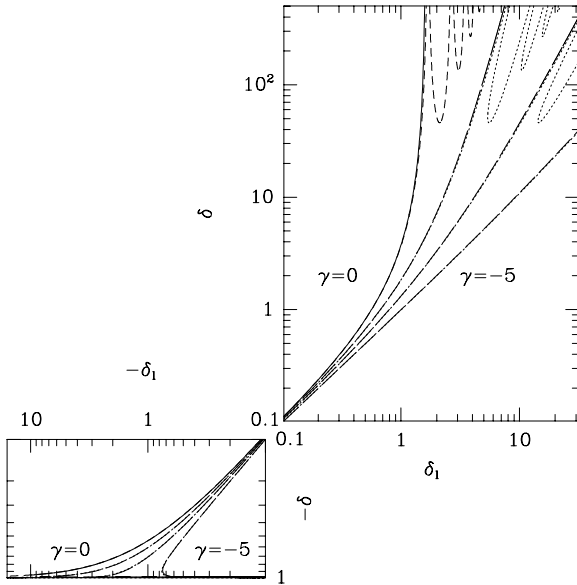


Figure A1. Local mappings for positive (top right-hand corner) and negative fluctuations (bottom left-hand corner). The short-dashed line shows the (unsmoothed $\gamma = 0$) spherical collapse (SC) result, which has a first bounce at $\delta_L \simeq 1.69$. The continuous line (which almost covers the short-dashed line) is the GZA with $\alpha = 21/13$ dimensions, which becomes singular at $\delta_L \simeq 1.62$ and has its first two derivatives equal to those of SC. The three long dashed lines below show the same GZA smoothed with increasing smoothing indices of $\gamma = -1.5, -3, -5$. These curves are difficult to distinguish from the corresponding SC mappings smoothed with the same γ , which are displayed as dotted-lines.

which is a symmetric version of the ZA in α dimensions and was also considered by Protogeris and Scherrer (1997). The case $\alpha = 3/2$ was introduced by Bernardeau (1994) as a good approximation to the SC model in the weakly non-linear regime. This value of α gives $\nu_2 \simeq 1.67$ in equation (A1), compared to the exact value $\nu_2 = 34/21 \simeq 1.62$. Here we will concentrate instead on the case $\alpha = 21/13$, as it reproduces exactly the SC result to second order: $\nu_2 = 34/21$, and therefore gives the exact skewness, $S_3 = 34/7$. This value of α also is a better approximation than $\alpha = 3/2$ around the singularity in δ , which occurs for $\delta_L = \alpha \simeq 1.62$, closer to $\delta_L \simeq 1.689$ than $\delta_L = \alpha = 1.5$. The higher order derivatives for the case $\alpha = 21/13$ are $\nu_3 \simeq 3.62$, $\nu_4 \simeq 10.35$ and $\nu_5 = 35.99$, which should be compared to the SC values in equation (A4). Another model of interest is $\alpha = 3/5(3\pi/2)^{2/3} \simeq 1.686$ which reproduces the behaviour exactly around the singularity, and gives $\nu_2 \simeq 1.59$, which is closer to the PT value in the SC than $\alpha = 3/2$.

The velocity divergence, equation (A7), in the GZA has the simple form:

$$\theta = -f_\Omega \delta_L \rho^{1/\alpha} = -f_\Omega \delta_L \left| 1 - \frac{\delta_L}{\alpha} \right|^{-1} \quad (\text{A11})$$

An important problem with these relations is that there is more than one value of δ_L for a given value of δ . This might be important when it comes to obtaining the PDF of δ . In practice this branching problem can be solved by assigning to δ the probability associated with the different branches in δ_L . However, we have checked that this is not important for

smoothed fields and this allows us to ignore this branching problem from now on.

A2 Smoothing effects

The above local relations correspond to unsmoothed fluctuations. We will focus instead on fields smoothed with a top-hat filter, defined as,

$$W_{TH}(\mathbf{x}, R) = 1 \quad \text{if } |\mathbf{x}| \leq R,$$

and zero otherwise, where R is the smoothing radius. The volume corresponding to radius R is $V = 4\pi/3R^3$. For top hat smoothing, the statistical properties of the smoothed fields can be obtained using the following prescription (see also Bernardeau 1994, FG98). Consider an initial (Lagrangian) fluctuation of infinitesimal mass m_0 extending over some volume $V_0 = 4\pi/3R_0^3$. The statistics of the IC must be given as an input to estimate the corresponding evolved, non-linear, values after gravitational growth. This is also true for the smoothed case, so that the shape and amplitude of the initial variance must be given or set 'by hand'. Consider first the case where we want the initial fluctuations smoothed within a radius R , to have a power-law variance:

$$\hat{\sigma}^2 = \sigma_0^2 \left(\frac{R}{R_0} \right)^\gamma, \quad (\text{A12})$$

where R_0 and σ_0^2 relates to the ‘‘unsmoothed’’ amplitude. In the linear regime, this sets the amplitude of linear fluctuations:

$$\hat{\delta}_L = D(t) \delta_0 \left(\frac{R}{R_0} \right)^{\gamma/2} = \delta_L \left(\frac{R}{R_0} \right)^{\gamma/2}, \quad (\text{A13})$$

where $D(t)$ is the gravitational growth factor and δ_0 is some (unsmoothed) initial seed whose variance is σ_0^2 , so that in the limit $R \rightarrow R_0$ we have $\hat{\sigma}_L^2 \rightarrow D^2 \sigma_0^2 = \sigma_L^2$.

On the other hand, in the local picture of evolution, a given fluid element m_0 is isolated, so that for a mean density \bar{n} , the smoothed overdensity is:

$$\hat{\rho} = \frac{m_0}{\bar{n}V} = \left(\frac{R_0}{R} \right)^3, \quad (\text{A14})$$

as the IC are perfectly homogeneous ($m_0 = \bar{n}V_0$), and the mean density \bar{n} does not change with time.

Putting the above equations together we have:

$$\hat{\rho} = \left(\frac{\delta_L}{\hat{\delta}_L} \right)^{6/\gamma}, \quad (\text{A15})$$

which shows that smoothing acts like a (implicit) Lagrangian mapping. Thus, given the unsmoothed mapping $\rho = \mathcal{G}(\delta_L)$, we can find the corresponding smoothed mapping by solving the implicit relation:

$$\hat{\rho} = \mathcal{G} \left[\hat{\rho}^{\gamma/6} \hat{\delta}_L \right], \quad (\text{A16})$$

where γ is the slope of the initial or linear smoothed variance:

$$\gamma = \frac{d \log \sigma_L^2}{d \log R}. \quad (\text{A17})$$

This can be easily generalized to non power-law relations and reproduces the original result of Bernardeau (1994).

The velocity divergence can be thought as a different δ_L mapping, i.e., equation (A7). Thus the smoothed results can be obtained as with equation (A16):

$$\hat{\theta} = \mathcal{G}_v[\hat{\delta}_L \rho^{\gamma/6}]. \quad (\text{A18})$$

A2.1 Smoothing in the SC model

In principle, the smoothing in ρ is difficult to implement analytically for the SC, because \mathcal{G} is given by the implicit relations Eqs.[A8]-[A9]. However, the smoothing can be carried out easily in terms of the smoothed δ_L , simply by noticing that from the above relation (equation [A15]) we have:

$$\hat{\delta}_L[\psi] = \frac{\delta_L[\psi]}{\rho[\psi]^{\gamma/6}}, \quad (\text{A19})$$

where ψ is such that $\hat{\rho} = \rho[\psi]$. The smoothed PDF of $\hat{\rho}$ will be given in terms of the smoothed PDF of the IC, which for a Gaussian field is also a Gaussian. So we just have, following Eq[9]:

$$P(\hat{\rho}) \propto \frac{P_{IC}(\hat{\delta}_L)}{\hat{\rho}} \left| \frac{d\hat{\delta}_L}{d\hat{\rho}} \right| = \frac{P_{IC}(\hat{\delta}_L[\psi])}{\rho[\psi]} \left| \frac{d\hat{\delta}_L}{d\psi} \right| \left| \frac{d\rho}{d\psi} \right|^{-1}, \quad (\text{A20})$$

with $\hat{\delta}_L[\psi]$ given by equation (A19). Care must be taken to use the correct relation, equation (A8) or equation (A9), depending on the sign of δ_L . For example, to estimate the moments of ρ we have:

$$\begin{aligned} \langle \rho^J \rangle &\equiv \int P(\hat{\rho}) \hat{\rho}^J d\hat{\rho} \\ &= \frac{1}{N} \int \frac{P_{IC}(\hat{\delta}_L^+[\psi])}{\rho^+[\psi]} \left| \frac{d\hat{\delta}_L^+}{d\psi} \right| \rho^+[\psi]^J d\psi + \\ &+ \frac{1}{N} \int \frac{P_{IC}(\hat{\delta}_L^-[\psi])}{\rho^-[\psi]} \left| \frac{d\hat{\delta}_L^-}{d\psi} \right| \rho^-[\psi]^J d\psi, \end{aligned} \quad (\text{A21})$$

where N is the normalization factor, so that $\langle 1 \rangle = 1$. The superscript $+$ denotes our use of equation (A8) and $-$ our use of equation (A9).

A2.2 Smoothing in the GZA model

From now on, unless stated otherwise, we use δ and ρ to refer to the smoothed fields. The unsmoothed case corresponds to $\gamma = 0$. The smoothed GZA mapping is given implicitly by equation (A16), which for the GZA case of equation (A10) yields:

$$\rho = \left| 1 - \frac{\delta_L \rho^{\gamma/6}}{\alpha} \right|^{-\alpha} \quad (\text{A22})$$

which nicely maps $\delta_L \in [-\infty, \infty]$ into $\rho \in [0, \infty]$. The resulting smoothed mapping for the GZA for $\alpha = 21/13$ and $\gamma = -2$ is shown in Fig. A1.

It turns out that for the GZA, even after smoothing, we can give analytical expressions for the PDF simply by using Eq[9] with:

$$\delta_L = \alpha \frac{\rho^{1/\alpha} - 1}{\rho^{\gamma/6 + 1/\alpha}}, \quad (\text{A23})$$

$$\left| \frac{d\delta_L}{d\rho} \right| = \frac{\rho^{-1/\alpha - \gamma/6} - \frac{\gamma}{6} \delta_L}{\rho}. \quad (\text{A24})$$

For example, for the evolved (smoothed) one-point PDF as a function of ρ , we have:

$$\begin{aligned} P(\rho) &= \frac{1}{N} \exp \left(- \left[\alpha \frac{\rho^{1/\alpha} - 1}{\rho^{\gamma/6 + 1/\alpha}} \right]^2 / (2\sigma^2) \right) \times \\ &\times \rho^{-1/\alpha - \gamma/6 - 2} \left(1 - \frac{\gamma}{6} \alpha [\rho^{1/\alpha} - 1] \right), \end{aligned} \quad (\text{A25})$$

for Gaussian initial conditions. These sort of compact relations were previously described by Protogeris & Scherrer (1997). Fig. 8 shows a comparison of the above PDF to the PDF from simulations and from the SC model.

The velocity smoothing can be obtained from equation (A18) and equation (A11):

$$\theta = -f_\Omega \delta_L \rho^{1/\alpha + \gamma/6} = -f_\Omega \delta_L \left| 1 - \frac{\delta_L}{\alpha} \right|^{-1} \quad (\text{A26})$$

Note that although the SC and the GZA give a good approximation to gravitational dynamics for small δ , it is likely and expected that these approximations break at some stage for large fluctuations. As mentioned before, this break is not likely to be important for our present purposes, as the statistics of the absorption features in the Ly α forest are dominated by the small fluctuations.